Universidade de Aveiro Departamento de Engenharia Cerâmica e do Vidro
2010

Bahadirov Kudrathon

Laminagem assimétrica do alumínio 1050

Asymmetric rolling of aluminum 1050

Universidade de Aveiro Departamento de Engenharia Cerâmica e do Vidro
2010

Bahadirov Kudrathon

Laminagem assimétrica do alumínio 1050

Asymmetric rolling of aluminum 1050

Dissertação apresentada à Universidade de Aveiro para cumprimento dos requisitos necessários à obtenção do grau de Mestre em Ciência dos Materiais, realizada sob a orientação científica da Dr. Augusto Luís Barros Lopes, Professor Auxiliar do Departamento de Engenharia Cerâmica e do Vidro da Universidade de Aveiro.

Dissertation presented to University of Aveiro for the requirement of partial fulfillment of the Masters of Science degree in materials science under supervision of Dr. Augusto Luís Barros Lopes, Auxiliary Professor in the Department of Ceramic and Glass Engineering of the University of Aveiro

o júri

presidente Prof. Dr. Joaquim Manuel Vieira, Prof. Catedrático, Universidade de Aveiro

Prof. Dr. Manuel Fernado Gonçalves Vieira, Prof. Associado, Universidade do Porto

Prof. Dr. Augusto Luís Barros Lopes, Prof. Auxiliar, Universidade de Aveiro

Prof. Dr. Mikael Larsen, Prof. Auxiliar, Aalborg Universitet

acknowledgements

I am very thankful to thank my supervisor Prof. Augusto Luís Barros Lopes for his guidance and support from the initial to the final stage enabled me to develop an understanding of the subject and writing the thesis.

I am grateful Dr. Gabriela Tamara Vincze for her assistance during all mechanical experiments and useful advice and Saeed Tamimi for his helpful suggestions in processing the obtained mechanical results.

I would also like to thank the EMMS consortium for the unforgettable program and the European Commission for the scholarship.

palavras-chave laminagem asimétrica, alumínio, textura cristalográfica, microestrutura de deslocações, anisotropia plástica, formabilidade de chapas metálicas.

resumo

Neste trabalho foi investigada a laminagem convencional e a laminagem assimétrica de chapas de alumínio 1050. Foram estudados três tipos diferentes de laminagem: laminagem convencional, laminagem assimétrica contínua e laminagem assimétrica com inversão da direcção de laminagem. A influência da orientação cristalográfica dos grãos e da estrutura de deslocações desenvolvidas durante a deformação plástica no comportamento mecânico do material foi analisada utilizando difracção de raios x e microscopia electrónica de transmissão. O modelo viscoplástico auto-coerente foi utilizado para quantificar o efeito da textura cristalográfica na evolução das curvas tensão-deformação obtidas em tracção uniaxial nas amostras após laminagem e tratamento térmico.

Os resultados obtidos mostraram que a laminagem assimétrica promove a deformação de corte ao longo da espessura da chapa e o desenvolvimento de componentes de textura de corte que são preservados durante o tratamento térmico. Estes componentes de textura, não gerados por laminagem convencional, conduziram ao aumento do coeficiente de anisotropia normal e da formabilidade da chapa metálica.

Um aumento da tensão de escoamento foi também observado em todas as amostras laminadas e tratadas termicamente. Este efeito foi atribuído ao refinamento do grão associado ao desenvolvimento de uma estrutura constituída por sub-grãos com 1-2 μm de tamanho.

keywords asymmetric rolling, aluminum, crystallographic texture, dislocation microstructure, plastic anisotropy, metal sheet formability

abstract

In this work asymmetric and conventional rolled 1050 aluminum alloy sheet was investigated. Three different types of rolling were studied: conventional rolling, asymmetric rolling continues and asymmetric rolling reverse. The influence of crystallographic orientation of the grains and dislocation structure developed during plastic deformation on the mechanical behavior of the material was analyzed using X-ray diffraction and transmission electron microscopy. The visco-plastic self consistent model was used to quantify the effect of crystallographic texture on the stress-strain curves obtained in tensile tests performed on the rolled samples before and after heat treatment.

The results showed that the asymmetric rolling produces shear strain along the thickness of the sheet that leads to development of crystallographic texture shear components that was preserved after annealing. These texture components, not generated in conventional rolling, led to an increase of the normal anisotropy coefficient and the formability of the metal sheet.

Increase of flow stress was also observed in all rolled and heat treated samples. This effect was attributed to grain refinement with development of sub-grain structure with 1-2 μm size.

Contents

List of figures

Symbols and abbreviations

r - reduction in thickness;

t_0 and t_f - the thickness of the strip before and after rolling, respectively;

υ - strips' speed;

$\dot{U}$ - roller's speed;

σ_{xf}, σ_{xb} – front and back tension on the strip;

L_p - the projected contact arc length between rolls and the processed material;

R_0 - rolling radii (when the rollers radii are the same);

P_r - rolling load;

p - specific pressure;

b - width of the strip;

F - friction force;

μ - friction coefficient;

R_1 and R_2 - the radii of the upper and lower rolls (when the rollers radii are different);

τ - shear stress;

V_1 and V_2 - circumferential speeds of upper and lower rolls

τ^s - magnitude of shear stress in a slip system s;

x^s – stands for a slip system;

m – Schmid factor;

τ_c^s - critical resolved shear stress;

ρ - dislocation density;

α' - average intensity of dislocation interactions;

b - Burgers vector of the dislocations;

θ_h - hardening rate;

ε - true strain;

σ - true stress;

γ - shear strain

M – Taylor factor;

$\varphi_1, \Phi, \varphi_2$ - Euler angles;

R – anisotropic coefficient;

$\overline{R}$ – normal anisotropic coefficient;

ΔR– planar anisotropic coefficient;

ε_{22} and ε_{33} - the width and thickness true strains;

w_0 and w - the initial and final width

β - distortion angle;

FCC – face centered cubic;

CR – conventional rolled (or rolling);

ASRC – asymmetric rolling continuous;

ASRR – asymmetric rolling reverse;

SPD – severe plastic deformation;

ECAP - equal channel angular pressing;

RD – rolling direction;

ASTM - American Society for Testing Materials;

VPSC – visco-plastic self consistent;

TEM - transmission electron microscope;

1 Introduction

Large fractions of metals are processed by rolling. In case of metal sheet rolling, the main objectives are the reduction of sheet's thickness until the desired dimension and the improvement of the mechanical properties of the material.

In many important industrial applications, as automotive, aircraft, construction, engineering and packing, the aluminum alloy sheets are used in large scales because of their properties, such as low density and high corrosion resistance. However, the high cost, the limited formability and the relatively low strength are the major drawbacks to wider-scale applications of aluminum components.

Formability of aluminum sheets depends mainly on the strain hardening changes during plastic deformation and anisotropy coefficient (R), i.e. width-to-thickness reduction ratio in uniaxial tensile test, which depends on the crystallographic texture of the material. Higher R values mean that the sheet deforms with less thickness reduction and presents higher formability. Theoretical calculations and experimental results have shown that the increment of R values can be achieved through the development of shear texture components by asymmetrical rolling. Another potential advantage of asymmetrical rolling is an increment of material's strength by grain refinement.

The objective of this work is to investigate the effect of asymmetric rolling on mechanical properties of 1050 aluminum sheets, in particular on the anisotropy coefficient values and on the material's strength.

The thesis is organized in five chapters, being the Introduction the first one.

In chapter 2 is presented a bibliographic review, where the main aspects of rolling, plastic deformation, crystallographic texture, dislocation structures, grain refinement and formability of sheet metals are presented.

Chapter 3 describes the initial material, experimental work and used techniques for characterization.

Chapter 4 provides the obtained results and their discussion.

In chapter 5 and 6 are presented the conclusions and proposals for future work.

2 Bibliographic review

2.1 Strip rolling

The strip rolling is the simplest type of rolling among variety of different ones. In this process the metal passes through the gap between cylindrical rollers, and its thickness is reduced by plastic deformation. This is performed by applying a force to the strip trough rollers' surfaces while the metal sheet moves through the rollers gap.

Concerning processing temperature, the process can be classified as hot, warm and cold rolling. If the temperature in working zone is higher than the material's recrystallization temperature the process is called hot rolling. When the temperature lower than recrystallization temperature of rolled metal is considered as warm or cold rolling.

Besides the shape modification of the strip, the materials' mechanical properties are changed by rolling as a result of plastic deformation.

2.1.1 Strip rolling analysis

During the rolling process, the energy is transferred from rolls to the strip trough the friction between cylinders and material's surfaces. While the strip passes between the gap of rolls, its thickness is uniformly reduced, the length is increased while its width remains almost unchanged. The reduction in thickness (r) can be calculated by the following expression [1]:

$$r = \frac{t_0 - t_f}{t_0}, \tag{2.1}$$

where t_0 and t_f are the thickness of the strip before and after rolling, respectively.

The elongation causes differences of speed of the material along the strip; the speed is higher at the exit than at the entrance of the gap between rolls. The strip moves slower than the rolls at the entrance ($\upsilon_0 < \dot{U}$) and faster than the rolls ($\upsilon_f > \dot{U}$) at the exit (Fig. 1). The point where the speeds of the strip and rolls are equal ($\upsilon = \dot{U}$) is called a neutral or non-slip point [2]. The change of speeds in different regions is proportional to the change of the roll gap:

$$\frac{\upsilon_f}{\upsilon_0} = \frac{t_0}{t_f}. \tag{2.2}$$

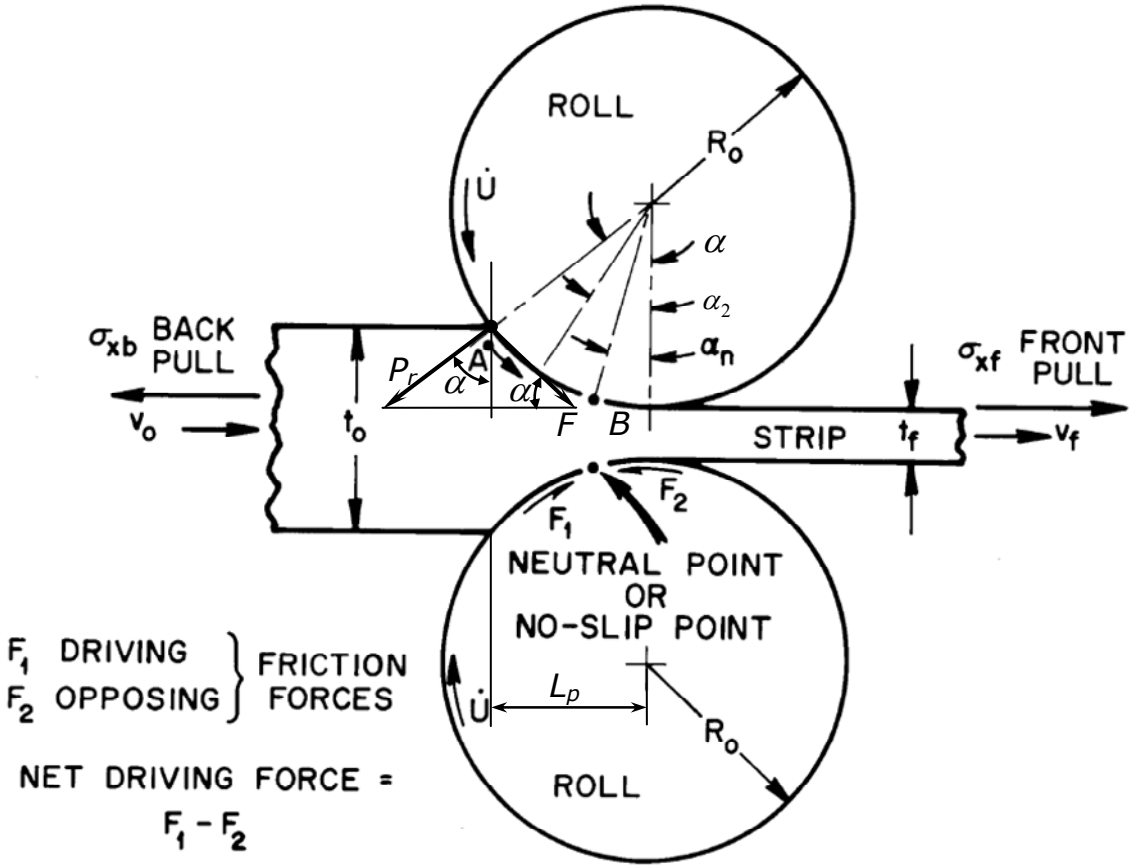

Fig. 1. Schematic view of strip rolling, neutral point and friction directions [2] (σ_{xf}, σ_{xb} – front and back tension on the strip, $\dot{U}$ - Roll circumferential velocity)

In the region between the entrance and neutral point the friction force of the roll on the material surface (F_1) moves the strip forward, while friction force (F_2), that acts in the region between neutral point and the exit opposes to the movement of the strip. The difference of the opposing forces is the net friction drag force of the rolling process.

Depending on the net force's magnitude the neutral point's position varies. In conventional rolling conditions, the increment of reduction causes the increase of F_1 and the non-slip point moves towards exit. The net force can be increased until the F_2 equals to zero, i.e. the neutral point reaches the exit ($\upsilon_f = \dot{U}$). After this point the rolls will start skidding over the strip, the power is not transferred from the rolls to the strip and the strip movement will stop.

The projected contact arc length between rolls and the processed material (L_p) can be determined as [3]:

$$L_p^2 = R_0^2 - \left(R_0 - \frac{\Delta t}{2} \right)^2 . \quad (2.3)$$

When the reduction $\Delta t = (t_0 - t_f)$ is very small compared to the rolling radii R_0, the equation can be simplified to:

$$L_p \approx \left[R_0 \Delta t \right]^{1/2} . \quad (2.4)$$

The vertical component of radial load (P_r) is known as rolling load and is given by $P_r \cos\alpha$. In order to calculate specific pressure (p) on the contact area the following expression can be used [3]:

$$p = \frac{P_r \cos\alpha}{bL_p}, \quad (2.5)$$

where b is the width of the strip.

The vertical component of P_r varies by contact angle α. The maximum value is reached on the neutral point [3]. The typical distribution of rolling pressure is shown on Fig. 2.

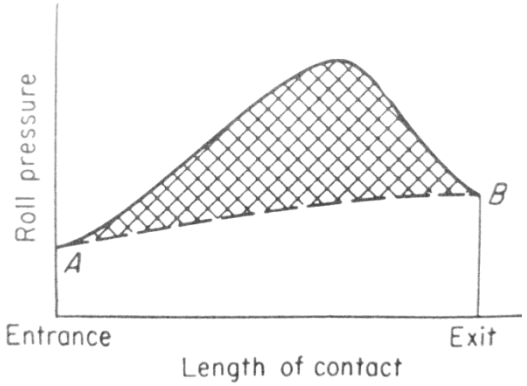

Fig. 2. Distribution of roll pressure (p) along the arc of contact [3]

In order to roll a strip, the rolls should not slip on contact surfaces of the sheet. This depends on the friction coefficient between contact surfaces, which can be described by the forces interacting in the system.

The projection of the friction force on horizontal axis ($F\cos\alpha$) should be bigger or equal to the rolling pressure projection on the same axis ($P_r \sin\alpha$):

$$F \cos \alpha \geq P_r \sin \alpha \,. \tag{2.6}$$

That can be rearranged as:

$$\frac{F}{P_r} \geq \frac{\sin\alpha}{\cos\alpha} \equiv \tan\alpha, \tag{2.7}$$

where F/P_r is, by definition, the friction coefficient μ:

$$\mu \geq \tan \alpha \,. \tag{2.8}$$

From the above equation it can be concluded that the value of $\tan\alpha$ bigger than friction coefficient causes the slipping of the piece against the rollers.

From Fig. 1, the relation between rolls radii, projected contact length and contact angle can be written as:

$$\tan\alpha = \frac{L_p}{R - \Delta t/2} \tag{2.9}$$

Replacing the L_p from eq. (2.4), it can be obtained

$$\tan\alpha \approx \frac{\sqrt{R \cdot \Delta t}}{R - \Delta t/2} \approx \sqrt{\frac{\Delta t}{R}}. \tag{2.10}$$

Substituting equations (2.8) with (2.10) shows that the maximum reduction depends on rollers radii and the friction coefficient [3]:

$$\Delta t_{\max} = \mu^2 R_0 \,. \tag{2.11}$$

2.1.2 Asymmetric rolling

Stripe rolling can be either symmetric (or conventional) or asymmetric. When the linear velocities, radii and surface friction coefficients of upper and lower parts of working cylinders are equal, the rolling is conventional.

Asymmetrical rolling occurs when any of the rolling parameter is distorted, for instance, difference in work rolls radii, rolls velocity or different friction parameters acting on both surfaces of the strip.

Differently from conventional rolling, in asymmetric rolling the neutral points do not have a position on a vertical line, they are shifted according to the asymmetry conditions (Fig. 3).

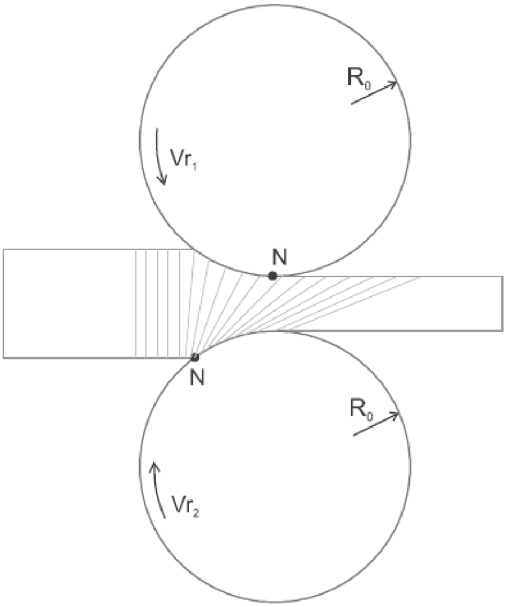

Fig. 3. Material flow and neutral points' positions in asymmetric rolling

2.1.3 Asymmetric rolling characteristics by slab method

As a result of volume reduction, the speed of stripe rapidly increases while passing through the rolling gap from entrance to exit. The speeds of stripe's surfaces are bigger than circumferential speeds of rollers at the exit and smaller at the entrance [1]. At neutral point the surface of slab and the roll speeds are the same. In conventional rolling the natural point location for each roll is symmetric. But in asymmetric rolling the neutral points of upper and lower rolls are located differently. In this case, the working zones of the roll gap can be divided into three parts from entrance point to the first neutral point (zone I), from latter to the second neutral point (zone II) and from the second neutral point until the exit (zone III), as shown on Fig. 4.

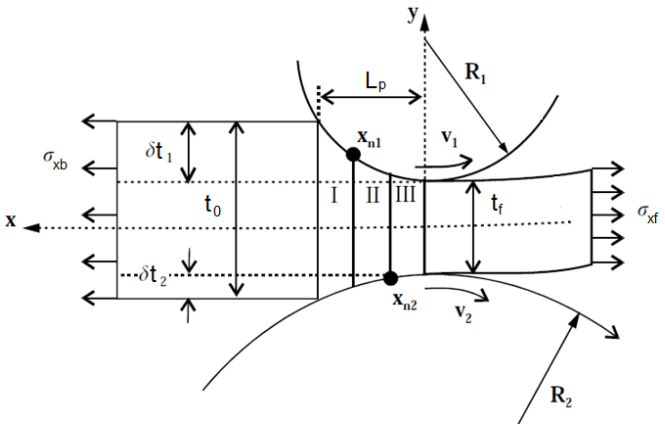

Fig. 4. Definition of three zones in asymmetric rolling [4]. R_1 and R_2 are the radii of the upper and lower rolls whereas V_1 and V_2 are circumferential speeds of upper and lower rolls. δt_1 and δt_2 are the thickness reduction under the rolls, L_p is projected contact length. t_i and t_0 are the initial and rolled thickness of the stripe. σ_{xb} and σ_{xf} represent front and back tension stresses

In zone I, the strip velocity is lower than the speeds of both upper and lower rolls and the frictional stresses on both surfaces move the material forward. In zone II, as the neutral points are not located on the same vertical line, the speed of upper roll is lower than the strip and, oppositely, the speed of the lower roll is higher than the latter. As a result, the friction stress on the upper side of the strip is backward and on lower side is forward, which gives a rise to shear strain through the strip thickness. In the zone III the friction stresses are backward and the speed of the strip is higher than of both rolls. These forces acting on the different zones are schematically shown in Fig. 5.

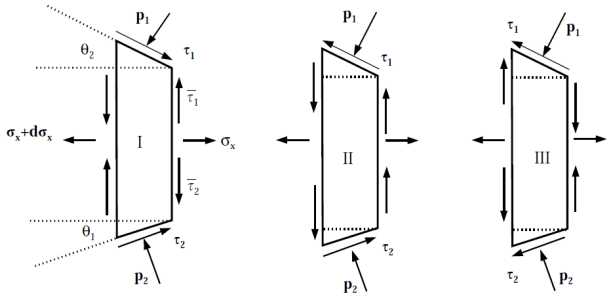

Fig. 5. Stress system acting at the three zones in asymmetric rolling. p_1 and p_2 are radial pressures of upper and lower rolls, respectively; τ_1 and τ_2 are the shear stresses acting on the material's surfaces [4]

Asymmetric rolling is being studied with a high interest in the last decades because of several advantages over conventional rolling, such as improved sheet surface finishing, reduction of rolling energy [4][5][6] (Fig. 6).It can be used to modify the material's properties by taking benefit of the shear strain imposed through the strip thickness [4][7].

Indeed, several studies [6][8][9][10][11] have shown that this additional shear strain contributes to grain rotation and subdivision producing grain refinement and modification of crystallographic texture of the material that can improve the properties of the sheet during subsequent plastic deformation process.

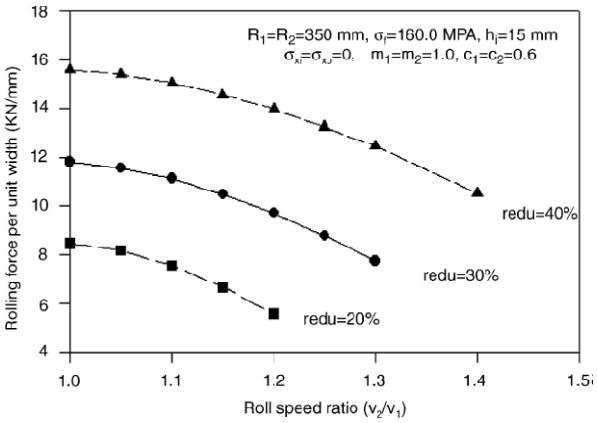

Fig. 6. Variation of rolling force per unit width with roll speed ratio for various thickness reductions [4]

2.2Plastic deformation mechanisms

2.2.1 Plastic deformation of single crystal

Plastic deformation is a type of deformation at which, after releasing the load, the deformed body does not recover its initial shape.

Usually the plastic deformation, at room temperature, of most metallic materials occurs through non-diffusive mechanisms, such as slip (in metals with high stacking fault energy, like aluminum) and twinning (in metals with low stacking fault energy) [12].

Slip occurs by multiplication and movement of dislocations along the planes and directions of the crystal lattice with the highest atomic density producing displacement of one crystal part over another (Fig. 7), as a result of an applied shear stress (τ).

In cubic metals with the face centered (FCC) lattice, as aluminum, these planes and directions are the {111} and <110>, respectively.

For a single crystal, the magnitude of the shear stress (τ^s) in a slip system *s* (defined by one slip plane and one slip direction) is given by:

$$\tau^s = \sigma^s \cos(\phi^s)\cos(\lambda^s), \qquad (2.12)$$

where σ is the applied stress, ϕ is the angle between the direction of σ and the normal to the slip plane and λ is the angle defined by direction of σ and the slip direction. The product $\cos(\phi^s)\cos(\lambda^s)$ is the Schmid factor m^s of the slip system:

$$\tau^s = m^s \sigma^s . \tag{2.13}$$

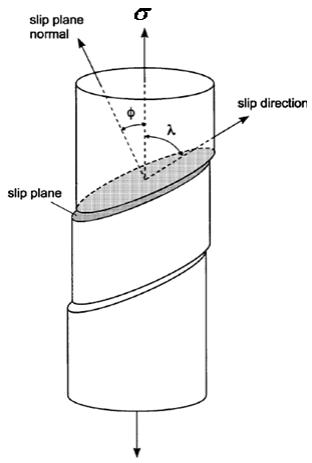

Fig. 7. Single crystal slip [12]

According to the Schmid law [13] yield will occur on a slip system *s* when the shear stress τ^s reaches a critical value τ_c^s *(critical resolved shear stress)*, i.e. [10]:

$$\begin{cases} \tau^s = \tau_c^s - slip\ \ system\ \ \ s\ \ is\ \ active \\ \tau^s < \tau_c^s - slip\ \ sytem\ \ \ s\ \ is\ \ latent \end{cases}$$

The value of τ_c^s (and therefore the value of flow shear stress - τ) depends on the friction stress for dislocation movement (τ_0) and its density (ρ) through the equation:

$$\tau_c^s = \tau_0 + \alpha' \mu b \sqrt{\rho} , \tag{2.14}$$

where α' represents the average intensity of dislocation interactions, μ is the shear module and *b* is the magnitude of Burgers vector of the dislocations.

2.2.1.1 Mechanical behavior

Studies of FCC single crystal's slip deformation under different conditions revealed that the shear stress-strain curve could be divided in three different stages (Fig. 8). The length of each stage depends on the orientation of crystal, temperature and strain rate imposed during the test [12][14][15].

For a single crystal initially orientated for a single slip, the stage I, is characterized by a low hardening rate ($\theta_h = d\tau / d\varepsilon$).

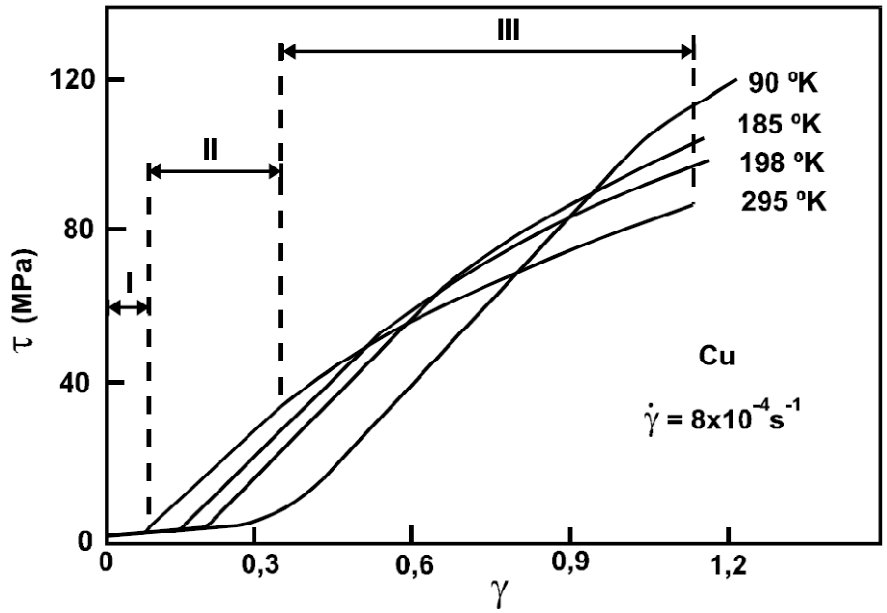

Fig. 8. Shear stress (τ) - strain (γ)curves of copper single crystal at different temperatures [14]. $\dot{\gamma}$ is shear strain rate

The beginning of stage II is characterized by a linear increase of the hardening rate due to the activation of other slip systems and to the increase of dislocation density.

The last stage occurs after the linear hardening behavior and is characterized by a parabolic hardening due to a dynamic recovery process as a result of mutual annihilation of dislocations. Unlike the previous stages, the beginning of this stage and the hardening evolution strongly depends on the temperature and strain rate.

2.2.2 Polycrystal models of plastic deformation

Modeling the mechanical behavior of polycrystalline materials from the responses of their single crystals has been a challenging task. Polycrystals consist of grains which, due to mutual interaction, cannot deform freely as single crystals. The compatibility process of

deformation between neighbor grains leads to the development of local accommodation stresses and to the differences between macroscopic and microscopic imposed strain/stress states.

Different mathematical models have been proposed to correlate the strain/stress in the polycrystal and in each grain [16][17][18][19].

2.2.2.1 Sachs model

The Sachs model assumes that all gains of the polycrystal undergo the same macroscopic stress. In this model the grains are treated as if they were an array of free single crystals, which can deform independently [20][21][22]. It is assumed that the plastic deformation is accommodated in each grain by the activation of the slip system with the highest Schmid factor, as proposed by Schmid law (eq. 2.13).

In this case, taking into account the different crystallographic orientation of the grains, the macroscopic applied stress to the polycrystal (σ) is given by:

$$\sigma = < m^{-1} > \widetilde{\tau} \,, \tag{2.15}$$

where $< m^{-1} >$ is the average of inverse Schmid factor and $\widetilde{\tau}$ is the average shear stress acting on the grains.

2.2.2.2 Taylor model

The Taylor model assumes that all the grains of the polycrystal undergo the same homogeneous strain as the polycrystal, keeping the continuity of the grain boundaries [20]. This homogeneous strain requires the activation of, at least, five independent slip systems. The set of five slip systems effectively activated in each grain is the one that minimizes the deformation energy.

$$(W_{\text{int}})_{\min} = \left(\sum_{s=1}^{S} \tau_c^s \left| \gamma^s \right| \right)_{\min} , \tag{2.16}$$

where $(W_{\text{int}})_{\min}$ represents the minimum internal work to deform the polycrystal and τ_c^s, γ^s are, respectively, the critical resolved shear stress and shear strain in slip system *s*.

From the equivalence between internal and external works, the last expression can be formulated in the following way [22][23]:

$$\sum_{i,j=1}^{3} \sigma_{i,j}\varepsilon_{i,j} = \left(\sum_{s=1}^{S} \tau_c^s \left| \gamma^s \right| \right)_{\min} . \tag{2.17}$$

Assuming that $\tau = \tau_c^s$, i.e. the critical resolved shear stress is independent on the slip system one obtains:

$$\frac{\sigma}{\tau} = \frac{\left(\sum_{s=1}^{S} \left| \gamma^s \right| \right)_{\min}}{\varepsilon} = M, \tag{2.18}$$

where σ, ε are the macroscopic stress and strain respectively. *M* is Taylor factor which depends on the orientation of the grains with respect to applied stress tensor.

Taking into account the crystallographic orientation of all grains of the polycrystal:

$$\sigma = < M > \tilde{\tau} , \tag{2.19}$$

where $< M >$ is the average Taylor factor and $\tilde{\tau}$ is the average shear stress.

The application of this model to simulate the polycrystal mechanical behavior is limited by the ambiguity in the selection of the activated slip systems, when more than one combination of five independent slip systems are solution of the equation 2.16.

2.2.2.3 Self-consistence model

In the Sachs model, the stress is assumed to be homogeneous and neighbor grains do not interact with each other. In the Taylor model, the deformation of the grains is fully constrained, and the strain is the same in all grains and equal to the macroscopic strain.

These approaches define the lower and upper bounds of the polycrystal mechanical behavior. The self-consistent model considers each grain as an inclusion in a homogeneous matrix. The properties of the matrix are the weighted averages over all grains orientations, according to the crystallographic texture of the polycrystal [10][24][25]:

$$E = < \varepsilon > , \tag{2.20}$$

$$\Sigma = < \sigma > , \tag{2.21}$$

here $< \varepsilon >$ and $< \sigma >$ are the average strain and stress on the individual crystals, E and Σ are the macroscopic stress and strain applied to the polycrystal.

There are several proposed equations that relate these parameters [26][27]. One of the most well succeeded interaction equation based on the inclusion formalism was proposed by Hill [28][29]:

$$\sigma - \Sigma = -L^H (\varepsilon - E) , \tag{2.22}$$

where L^H is called the Hill's constraint tensor that depends of the grain shape and crystallographic orientation of the grains.

2.2.2.4 **Viscoplastic model**

The viscoplastic model assumes that the shear strain rate in each slip system ($\dot{\gamma}^s$) depends on the resolved shear stress (τ^s) by the power law [10][30]:

$$\dot{\gamma}^s = \dot{\gamma}_c^s \left(\frac{\tau^s}{\tau_c^s} \right)^\eta , \tag{2.23}$$

where $\dot{\gamma}_c^s$ and τ_c^s are the reference shear rate and critical resolved shear stress on the system, respectively, and η is the inverse strain rate sensitivity coefficient of the material.

In this case all systems are activated (but with a different magnitude) and the ambiguity of Taylor model in the selection of the activated slip system is overcame.

2.2.3 Dislocation microstructure

During the plastic deformation, dislocations tend to arrange themselves inside the grains in high density areas, so-called dislocation walls, which delimit regions with low dislocation density. These volumes are called dislocation cells. The degree of organization depends on the accumulated strain and dislocation mobility.

The shape of the dislocation cells depends on the number of locally activated slip systems. If one or two slip systems are activated, one or two families of straight dislocation walls parallel to the traces of slip planes with highest activity are observed. If more than two slip systems are strongly activated they form equiaxial cells.

With the increasing of dislocation density during the plastic deformation, the cell size and wall thickness decrease. This progressive sharpening of the cell walls leads to the creation of high angle boundaries inside of each grain and different dislocation structure with increased crystallographic misorientation.

Because local stresses can change from point–to-point in each grain, as a result of compatibilisation processes of plastic deformation between neighbor grains. The dislocation microstructure can be heterogeneous, giving a rise to the grain subdivision and to different dislocation structure characteristics in different places of the grain.

2.2.4 Crystallographic texture

The crystallographic texture, i.e. the preferential crystallographic orientation of the grains in polycrystalline materials, induces anisotropy of properties.

For metallic materials the preferential orientation of the grains occurs during thermo-mechanical processes as solidification, cold or hot work processes, recrystallization, etc.

One of the most widespread forms of texture representation is by pole figures, which is a stereographic projection of the distribution density of the given {hkl} crystallographic plane normals.

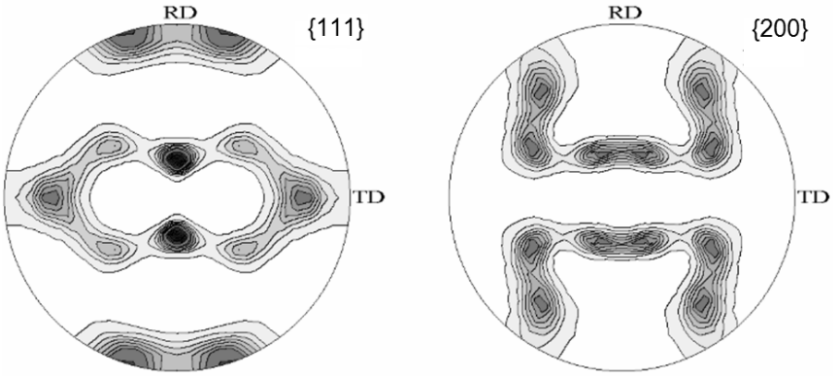

Fig. 9. Typical {111} and {200} pole figures of aluminum after conventional rolling. RD-rolling direction; TD-transverse direction

The most common technique for texture evaluation is the X-ray diffraction using special goniometer that allows to measure the diffracted intensity by {hkl} plane, for different orientations of the sample.

In the case of sheets, another way to express the preferential orientation of the crystals is through the identification of Miller indices of crystallographic plane {hkl} and direction <uvw> parallels to the sheet plane and rolling direction. For example, after recrystallization the Al sheets usually present {100}<001> preferential orientation, termed cube texture component. After conventional rolling, the typical components are Copper {112}<111>, S {123}<634> and Brass {011}<211>.

More detailed representation of grains orientation is through a set of three angles (Euler angles: $\varphi_1, \Phi, \varphi_2$) that put in coincidence of crystal axis (a, b, c) and the macroscopic specimen axis (X, Y, Z) (Fig. 10 and Fig. 11).

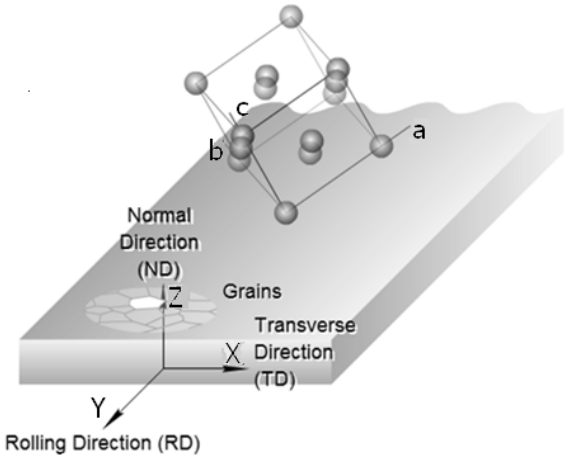

Fig. 10. Crystal axis (a, b, c) and macroscopic specimen axis (X, Y, Z) defined for a sheet [31]

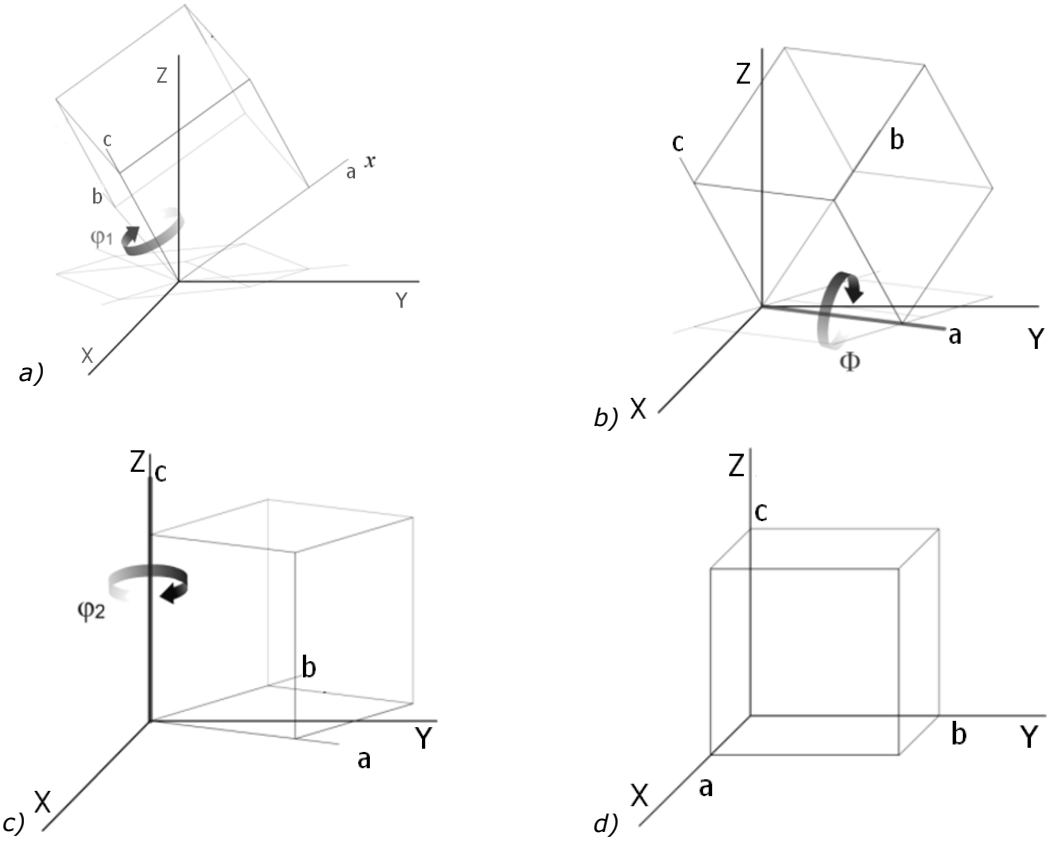

Fig. 11. Bunge's definition of Euler angles($\varphi_1, \Phi, \varphi_2$)[31]

Knowing the crystallographic orientation ($g=(\varphi_1, \Phi, \varphi_2)$), each crystal can be represented by one point in Euler space. For cubic crystals and no sample symmetry the range of angle is given by $0 \le \varphi_1 \le 2\pi$, $0 \le \Phi \le \frac{\pi}{2}$, $0 \le \varphi_2 \le \frac{\pi}{2}$. If the orthotropic sample symmetry is considered, a subspace is defined for $\varphi_1, \Phi, \varphi_2$ angles which range from 0 to $\frac{\pi}{2}$ (Fig. 12).

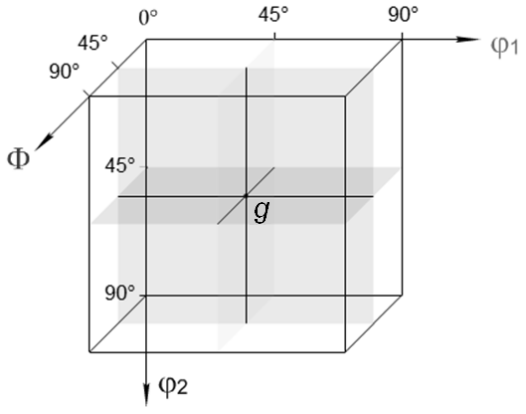

Fig. 12. Euler space [31]

Taking into account all the grains orientations, the texture of polycrystal can be represented in Euler space by 3D iso-surfaces (Fig. 13a). However this representation is complex to analyze and usually the texture is represented by 2D representations of Euler space at constant φ_2 (Fig. 13b).

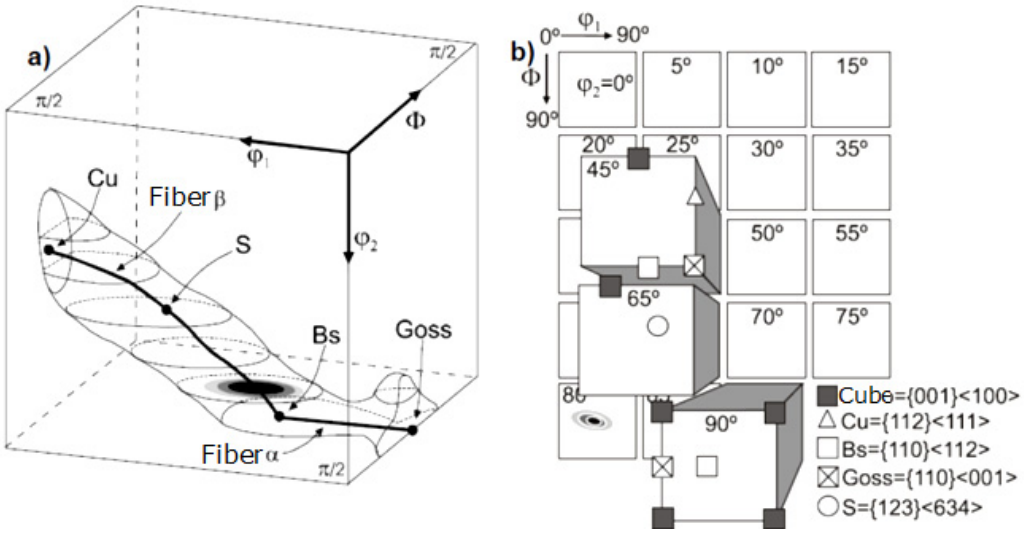

Fig. 13. Euler space representation of some typical texture components of FCC metals. a) Three-dimensional representation; b) two-dimensional representation of sections with constant values of φ2 [32]

2.2.5 Mechanical behavior

The mechanical behavior of polycrystals depends on the contribution of individual grains, taking into account their crystallographic orientations and local interactions due to the accommodation of deformation between neighbor grains.

One of the most important parameter to characterize the mechanical behavior of polycrystalline metals is the formability, defined as an ability to shape the metal by plastic deformation during the forming process.

Sheet metal formability is a complex issue in industrial production, where the main objective is to produce a part with specific requirements of shape, dimensions and appearance. The formability highly depends on the materials parameters such as crystallographic texture and grain size. Besides intrinsic factors of the material, formability of the metal also depends on several extrinsic parameters such as a strain path change strain rate, and forming temperature.

2.2.5.1 Crystallographic texture

The preferred orientation of grains causes anisotropy of plastic properties of metals [24], that can be characterized by Lankford parameter or anisotropy coefficient (R). This coefficient is determined by uniaxial tensile tests on sheet specimens and defined by:

$$R=\frac{\varepsilon_{22}}{\varepsilon_{33}}, \tag{2.24}$$

where ε_{22} and ε_{33} are the width and thickness true strains given by (Fig. 14):

$$\varepsilon_{22}=\ln\frac{w}{w_0} \text{ and } \varepsilon_{33}=\ln\frac{t}{t_0}, \tag{2.25}$$

w_0 and w are the initial and final width, while t_0 and t are the initial and final thickness of the specimen, respectively.

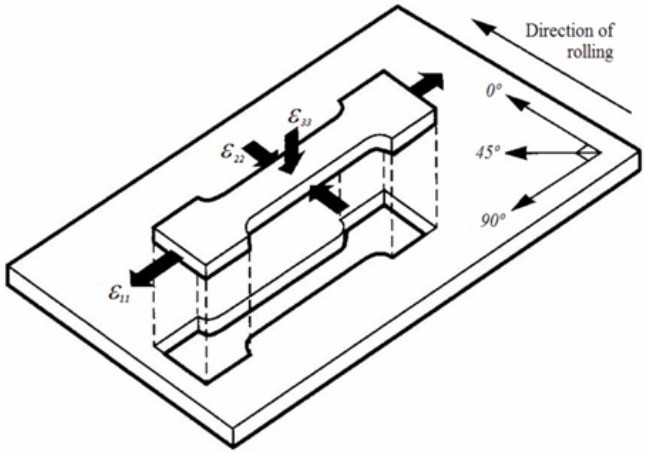

Fig. 14. Tensile test specimen of rolled sheet showing strain directions

The experimental measurement of sheet metal thickness change is difficult. Thus, considering that the deformation occurs at constant volume, ε_{33} is defined by:

$$\varepsilon_{33}=-(\varepsilon_{11}+\varepsilon_{22}), \tag{2.26}$$

where $\varepsilon_{11}=\ln(l/l_0)$, with l and l_0 are the final and the initial length of the sample, respectively. Therefore:

$$R = -\frac{\varepsilon_{22}}{\varepsilon_{11} + \varepsilon_{22}}. \tag{2.27}$$

The R-values usually differ with the direction defined in a sheet plane. In this case the mean plastic anisotropy of the sheet is expressed by the coefficient of normal anisotropy ($\overline{R}$), that is calculated from the R-values measured at 90°, 45°, 0° from the reference direction (usually rolling direction) using the equation:

$$\overline{R} = \frac{R_0 + R_{90} + 2R_{45}}{4}. \tag{2.28}$$

The variation of anisotropy coefficient with the angle on the sheet plane is given by the planar anisotropy coefficient (ΔR):

$$\Delta R = \frac{R_0 + R_{90} - 2R_{45}}{2}. \tag{2.29}$$

Higher values of $\overline{R}$ correspond to a higher capability of the sheet to deform before failing by excessive thickness reduction, i.e. they reflect a higher formability of the sheet (Fig. 15). The planar anisotropy ΔR is related to earring. Indeed, when $\Delta R \neq 0$ the final part will present "ears", as shown in Fig. 16.

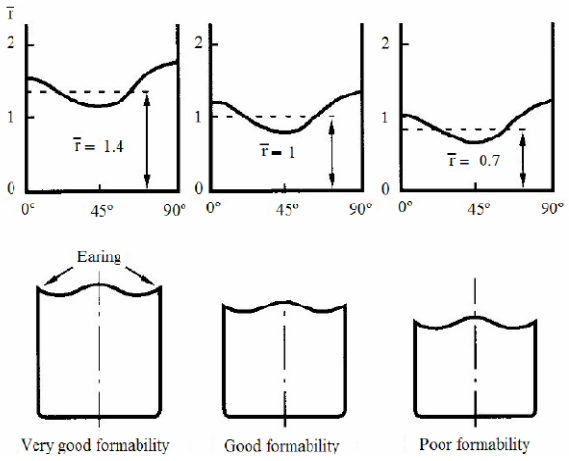

Fig. 15. Effect of $\overline{R}$ on formability for positive values of ΔR

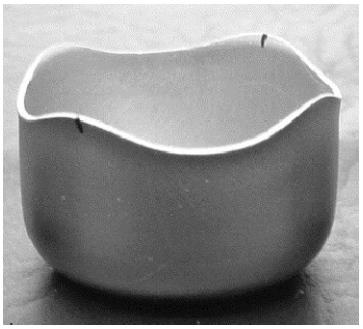

Fig. 16. Typical appearance of a deep drawn cup with ears [33]

The influence of the crystallographic texture on the $\overline{R}$ and ΔR values is well illustrated by the theoretical calculations performed by Choi, S. H. et al. [34], using a full-constrains Taylor model and a visco-plastic self consistent (VPSC) polycrystal models (Fig. 17).

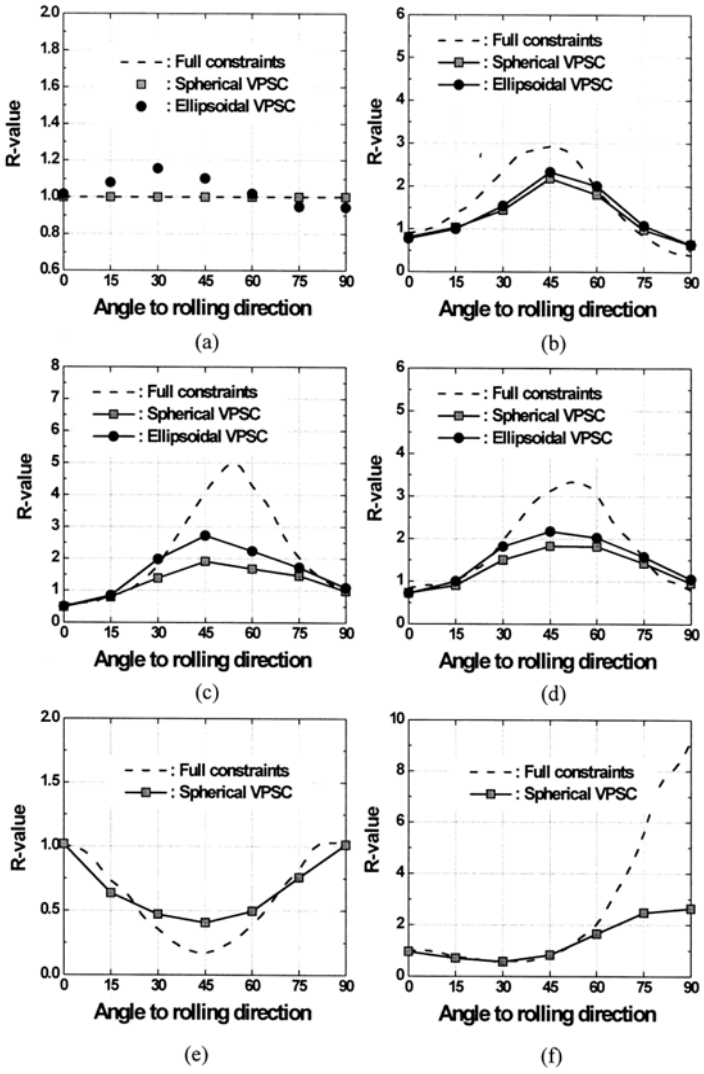

Fig. 17. Comparison of R-value directionality predicted by the Taylor (full constraints) and the VPSC models for six texture components. (a) Isotropic; (b) Copper; (c) Brass; (d) S; (e) Cube; (f) Goss [34]

2.2.5.2 Change of strain path

Depending on the final shape of the piece, metal forming processes usually involve large strains and changes of the loading mode and/or loading direction. These conditions lead to a temporary change of work hardening rate that can be a source of premature failure.

Especially, when softening is promoted, the strain localization can occur and the formability of the material reduces.

The effect of strain path change on the formability of sheet metal is usually represented by forming limit diagrams (FLD) (Fig. 18)

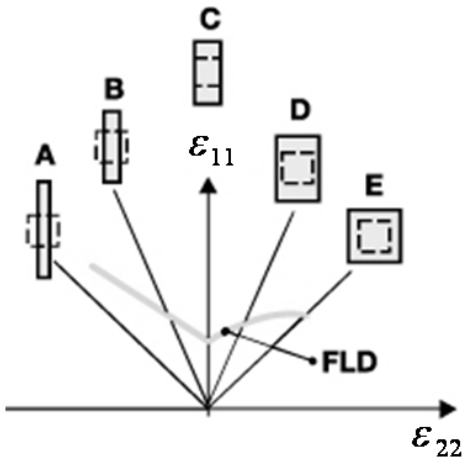

Fig. 18. Forming limit curve in true strain. A - Pure shear; B - Uniaxial tension; C - Plane strain; D - Stretch forming; E - Equibiaxial strain

The origin of this transient hardening behavior can be analyzed using the equation (2.19). Indeed, the flow stress during pre-strain (σ_p) can be expressed by:

$$\sigma_p = < M_p > \tilde{\tau}_p \qquad (2.30)$$

and at reloading:

$$\sigma_r = < M_r > (\tilde{\tau}_p + \Delta\tilde{\tau}) \,, \qquad (2.31)$$

where $<M_p>$ and $<M_r>$ are the average Taylor factor calculated from the crystallographic texture of the sample during the pre-strain and the reloading. The term $(\tilde{\tau}_p + \Delta\tilde{\tau})$ is the effective reloading shear stress due to dislocation interactions.

From equations (2.30) and (2.31):

$$\frac{\sigma_r}{\sigma_p} = \frac{< M_r >}{< M_p >}\left(1 + \frac{\Delta\widetilde{\tau}}{\widetilde{\tau}_p}\right), \tag{2.32}$$

where each term represents, respectively, the contribution of crystallographic texture and dislocation structure for the mechanical behavior during reloading.

In the last equation the shear change $\Delta\widetilde{\tau}$ depends on the amplitude of strain path change, which is characterized by α parameter [35]:

$$\alpha = \frac{\varepsilon_p \cdot \varepsilon_r}{\|\varepsilon_p\|\|\varepsilon_r\|}, \tag{2.33}$$

with ε_p and ε_r being the pre-deformation and reloading strain tensors, respectively. The value of α varies between 1 (no change of strain path: monotonic tests) and -1 (the inversion of strain paths: Bauschinger tests) and is related to the slip system activity. For $\alpha = 1$, the same slip systems are activated before and after reloading, and no change in the mechanical behavior is observed ($\Delta\widetilde{\tau} = 0$).

For $\alpha = -1$ the slip systems activated during the pre-strain are reactivated in opposed direction during the reloading and the material presents the typical mechanical behavior of curve (a) in Fig. 19 ($\Delta\widetilde{\tau} < 0$).

For $\alpha = 0$ occurs the activation of slip systems at reloading that were latent during the pre-strain. This requires higher reloading stress to initiate the movement of dislocations in the new slip systems ($\Delta\widetilde{\tau} > 0$) due to the low mobility of the pre-strain dislocation structure during the new deformation path (curves *b* and *c* in Fig. 19). After this initial stage, dislocation annihilation processes are activated and the pre-existing dislocation structure is replaced by the structure typical to the second loading. As a result, depending on the pre-strain value, transient softening occurs and can lead to the strain localization after the beginning of the reloading.

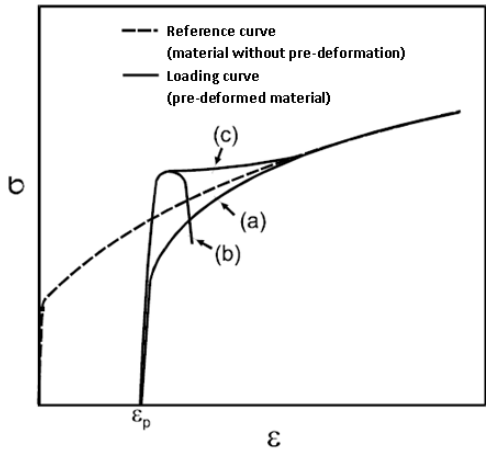

Fig. 19. Reloading stress-strain curves in tensile tests. σ-stress; ε-uniaxial tensile strain of pre-deformed materials; ε_p-pre-deformation [36]

2.2.5.3 Grain size

During the plastic deformation the grain boundaries act as obstacles to the movement of dislocation, and increase the stress level for the plastic deformation [30][37][38]. This explains the increase of yield stress (σ_0) when the grain size (D) decreases, as expressed by the Hall-Petch equation:

$$\sigma_0 = \sigma' + k\, D^{-1/2}, \tag{2.34}$$

where σ' and k are constants.

This means that reducing the grain size of metals to the submicron level can lead to significant improvements of their mechanical properties. Indeed, ultrafine-grained metals present higher strength [30],[39] and, under the appropriate conditions of strain rate and temperature, can present a super-plastic behavior, which is of great interest of the modern industries [40].

During the last decades, severe plastic deformation (SPD) methods have been proposed to produce grain refined bulk metals [30]. Some of most investigated techniques are the equal-channel angular pressing (ECAP) [41] and asymmetric rolling [42].

The ECAP method is used to obtain nanostructured materials with high morphological homogeneity of grains from the bulk of plastically deformed billets [40][43][44]. Deformation occurs when the sample is forced to pass through an intersection of two channels with the same cross section shape and area (Fig. 20). These produce a strong shear strain on the sample and the repetition of the process causes a gradual decrease of grain size by forming a sub-grain structure with increased crystallographic misorientation.

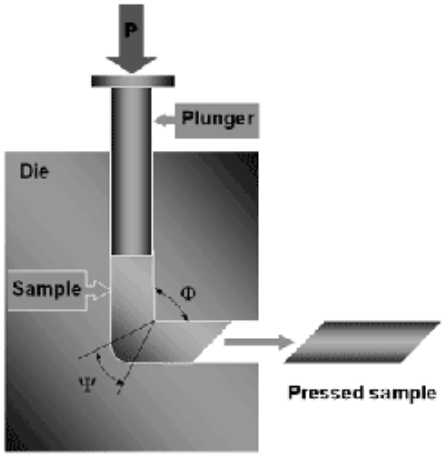

Fig. 20. Schematic sketch of ECAP process [45]

The intersection angle between channels is of great importance because it determines the amount of imposed shear strain and, consequently, the reduction of grain size and crystallographic texture of a sample. The proper lubrication, pass routes and geometry of the billet are also important parameters that should be controlled during ECAP process [46]. The process productivity can be increased by applying the ECAP with moveable channel walls which eliminates the friction on the walls.

Despite the ECAP process can produce ultrafine grained metal [47][48][49], this method is limited to the production of small pieces. For large scale grain size refinement of larger samples the asymmetric rolling is more suitable.

2.2.6 Asymmetric rolling

Under proper processing conditions the asymmetric rolling imposes a shear strain along the thickness of the sheet metal causing grain sub-division and rotation. Depending on the imposed strain amount, this can lead to the grain size refinement and the development of a texture typical to the shear deformation which is usually related to the improvement of sheet formability. This potential have been studied by several authors using different materials as aluminum [9][50][51][52][53][54][55], steel [56][57][58][59][60], magnesium [61][62], etc.

In the case of FCC materials, simulations of mechanical behavior based on crystal plasticity models showed that texture components {111}<110> and {111}<112>, produced by shear deformation, promote an improvement of anisotropy coefficients, when compared with the ones presented in conventionally rolled or recrystallized metals [63] (Table 1).

Table 1. Values of $\overline{R}$ and ΔR for most common crystallographic texture components in FCC material [63]

Designation	Miller indices {h,k,l} <u,v,w>	Euler angles			Predicted anisotropy		Texture type
		φ_1	Φ	φ_2	$\overline{R}$	ΔR	
C-Copper	{112}<111>	90	35	45	3.4	-5.7	Rolling texture components
S	{123}<634>	59	34	67	2.9	-5.1	
B-Brass	{011}<211>	35	45	0	4.7	-8.1	
D-Dillamore	{4 4 11}<11 11 8>	90	27	45	1.8	-3.3	
H	{001}<110>	0	0	45	0.5	-1	Shear texture components
E	{111}<110>	60	54.7	45	7.2	-0.5	
F	{111}<112>	90	54.7	45	7.3	-0.8	
Cube	{001}<100>	0	0	0	0.5	1	Recrystallization texture components
G-Goss	{110}<001>	0	45	0	15	30	
R	{124}<211>	53	36	60	1.9	-1.2	
P	{011}<112>	65	45	0	2.8	1.6	
Q	{013}<231>	58	18	0	0.54	-0.8	

Choi et al. [64] is one of the first who used the asymmetric rolling to produce shear texture components to improve the formability of aluminum. Later Kim et al. [65] reported an increase of $\overline{R}$ value from 0.87 (after conventional rolling and annealing) to 1.5 (after asymmetric rolling and annealing). However this improvement was followed by a strong increase of ΔR parameter from 0.01 to 1.32. Improvement of anisotropy coefficients was also reported by Sakai et al. [66], Utsunomia [54] on 5052 and 1050 aluminum alloy sheets, respectively, after asymmetric rolling and annealing at different temperatures (Fig. 21, Fig. 22)

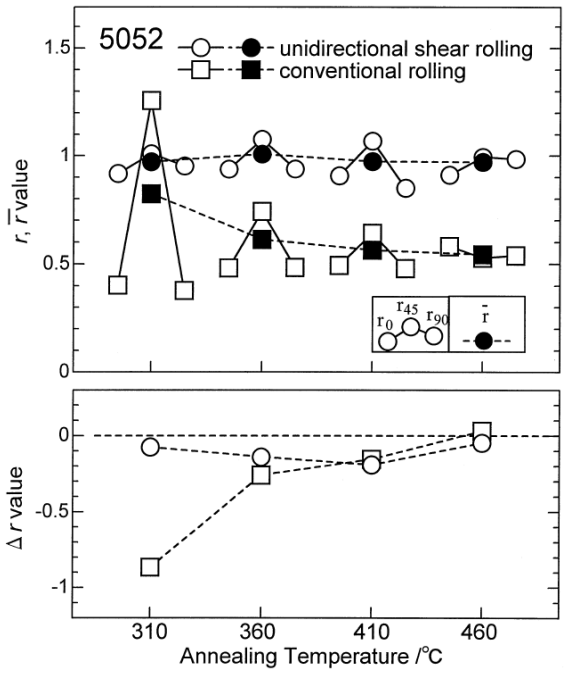

Fig. 21. Anisotropy coefficients of rolled and annealed Al 5052 sheets [66]

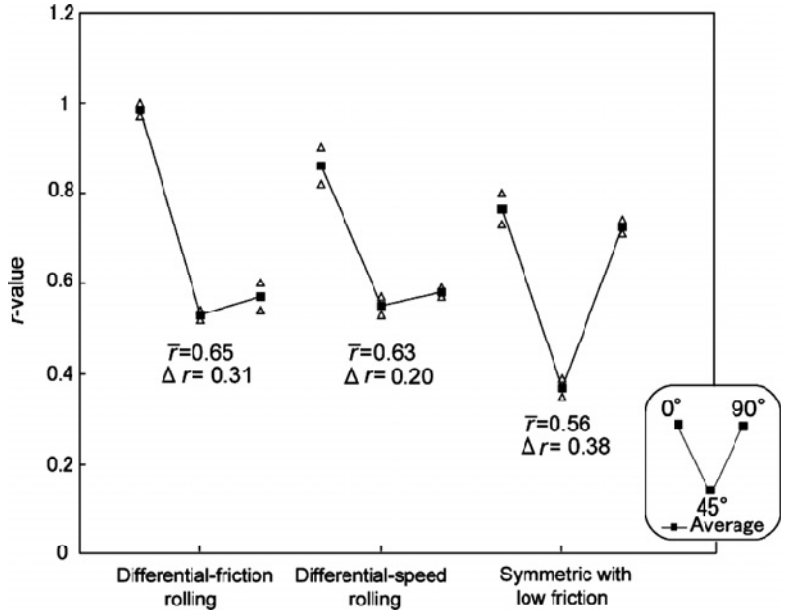

Fig. 22. Anisotropy coefficients of rolled and annealed Al 1050 sheets [54]

In another work, Kim et al. [8] concluded that the ideal shear deformation texture cannot be obtained by unidirectional asymmetric rolling (asymmetric rolling continuous - ASRC) but can be obtained by reversing the asymmetric rolling direction after each pass (asymmetric rolling reverse - ASRR).

The use of asymmetric rolling for achieving a grain refinement is another motivation to investigate this process. Indeed, grains with less than 2 μm produced by asymmetric rolling were reported by several authors [50][67][68].

Despite the increase of flow stress, significant decrease of uniform strain was observed in these studies. However, a good combination of strength and ductility can be achieved by heat treatment after asymmetric rolling [54][69][70].

The success of the use of asymmetric rolling to improve the formability and improve the material's strength depends on the amount of shear strain imposed during the process, which is a function of the rolling conditions (reduction per pass, number of passes, friction, roll speed ratio, initial thickness of the sheet, etc). For Al 1050 sheets these influences were studied by Simões [65], who reported a limited improvement in the mechanical properties of the material after asymmetric rolling due to a small amount of shear strain imposed during the deformation process.

3 Material and experimental methods

The main objective of this work is to investigate the effect of asymmetric rolling on the mechanical properties of 1050 aluminum sheets, in particular on anisotropy coefficients and on the flow stress. For that, the mechanical behavior of asymmetrically and conventionally rolled samples was characterized by uniaxial tensile tests in different directions of the sheet.

Texture measurements and TEM observations were performed after rolling and tensile tests in order to evaluate the effect, on the mechanical behavior of the sample, of the preferential crystal orientations and microstructures developed during the deformation. These analyses were complemented with calculations using a polycrystal plasticity model.

3.1 Initial material

The material selected for this work was a 1050 aluminum sheet with 3 mm initial thickness and the chemical composition given in the Table 2.

Table 2. Chemical composition of AA1050

Elements	Si	Fe	Cu	Mn	Mg	Cr	Ni	Zn	Ti	Ga	V
Amount, %	0,089	0,280	0,002	0,001	0,001	0,001	0,003	0,005	0,011	0,016	0,007

3.2 Rolling deformation

The asymmetric and conventional types of rolling of the material were performed in the house built device shown in Fig. 23. The machine has identical upper and lower cylinders with diameter 180 mm, powered with independent DC electrical motors. The rotation speeds of the rolls were controlled by computer using dedicated software. In conventional rolling experiments was used 15 rpm as a speed of both rolling cylinders. The asymmetric rolling was carried out using 5rpm and 15rpm, respectively, for lower and upper rolls.

a) 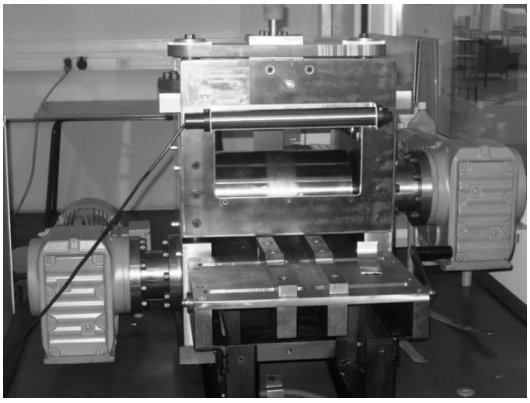 b) 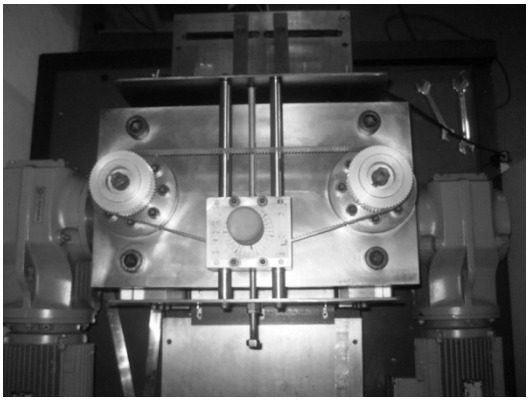

Fig. 23. Rolling device view from front (a) and top (b)

For all rolling experiments, the thickness reduction per pass was 15%, which corresponds (after 2, 4 and 6 passes) to 28%, 48% and 62% of total thickness reduction.

Conventional rolled (CR) samples were always rolled in the same direction. Asymmetric rolling was performed in two different sequences: asymmetric rolling continues (ASRC) and asymmetric rolling reverse (ASRR). In ASRC, the rolling direction (RD) was not changed. In ASRR, the samples were rotated 180° around RD after each pass (Fig. 26. b).

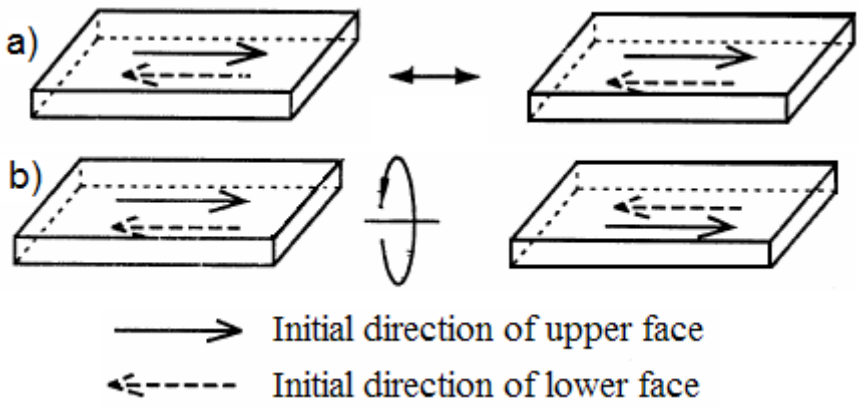

Fig. 24. Definition of rolling sequences for ASRC (a) and ASRR (b)

In order to keep the value of friction coefficient between rolls and sample surfaces high, no lubrication was used and the working surfaces of rolls were cleaned periodically.

After ASRC and ASRR experiments, was measured the distortion angle β of a vertical line (marked as showed in Fig. 25), which was used to calculate the macroscopic shear strain (γ) imposed during the asymmetric rolling:

$$\gamma = \tan(\beta) \qquad (3.1)$$

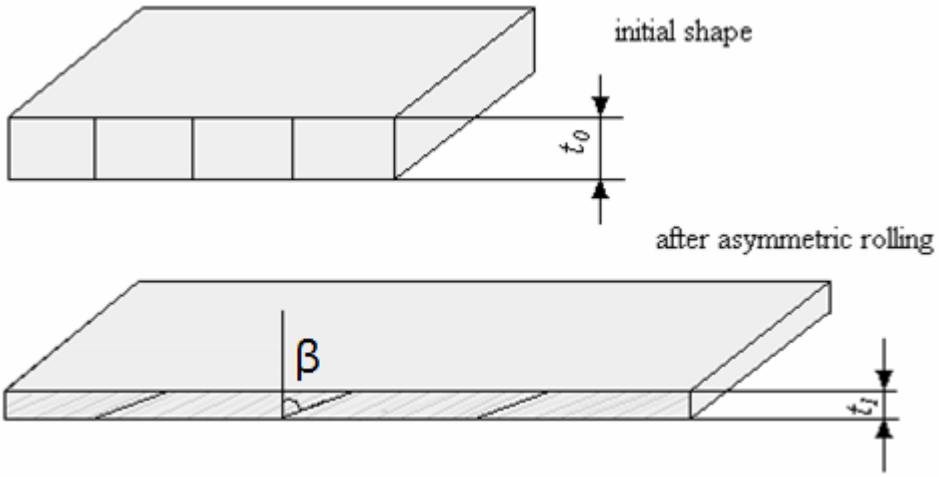

Fig. 25. Schematic representation of sample before and after asymmetric rolling

3.3Uniaxial tensile test

The mechanical properties characterization of samples before and after different rolling types was performed by uniaxial tensile test using an universal testing machine Shimadzu Autograph with maximum load capacity of 50 kN. The length and width changes were measured by a non-contact video extensometer MFA-25.

The ASTM tensile specimen with 10 mm width (Fig. 26) cut at 0°, 45°, 90° from RD were used. The tests speed was 1.5mm/min, which correspond to initial strain rate of $\dot{\varepsilon}=10^{-3}$ s^{-1}.

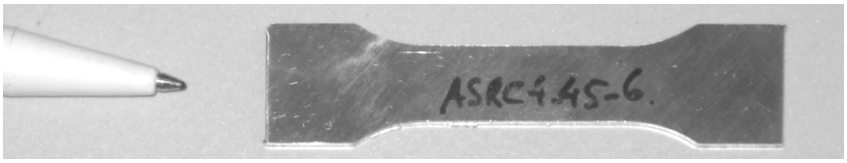

Fig. 26. ASTM tensile specimen with 10mm width

3.4Crystallographic texture analysis

The crystallographic orientation of the grains was characterized by measuring {200} and {111} X-ray pole figures using a Philips X'pert diffractometer equipped with texture goniometer (Fig. 27). Samples were polished until the middle of the thickness and the Cu K α radiation were used in these measurements.

The acquired data was processed by dedicated software using the MTEX MATLAB tool box [71]. From the processed pole figures, a set of 1000 weighted orientations were extracted

and used to compute the <M> value, using VPCS model code developed by Lebenshon and Tome [18][28][29].

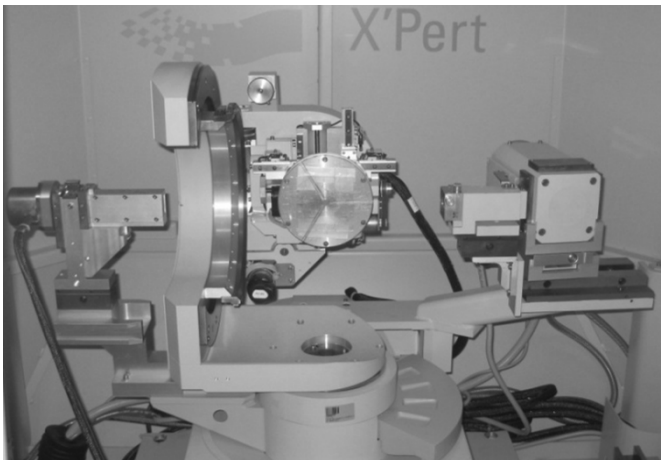

Fig. 27. Philips X-ray diffraction device with goniometer

3.5Transmission electron microscopy observations

The dislocation microstructure developed in the samples after deformation was characterized using a 300kV Hitachi H-9000 transmission electron microscope (TEM). TEM foils parallel to the sheet plane were taken at the sample's mid-thickness location. The samples were prepared by mechanical polishing of both sides and electropolished using a double–jet thinner with dilute solution of HNO_3 and methanol under 10 V, until perforation occurred.

4 Results and discussion

4.1 Initial material characterization

The uniaxial tensile true stress (σ) – true strain (ε) curves of as received material at θ=0°, 45° and 90° from initial rolling direction (RD) are presented in Fig. 28. It can be seen that, for the same strain value, the flow stress changes with the test direction. This anisotropic behavior results in differences up to approximately 10% of maximum tensile stress (σ_{max}) and uniform strain (ε_u) values (Table 3).

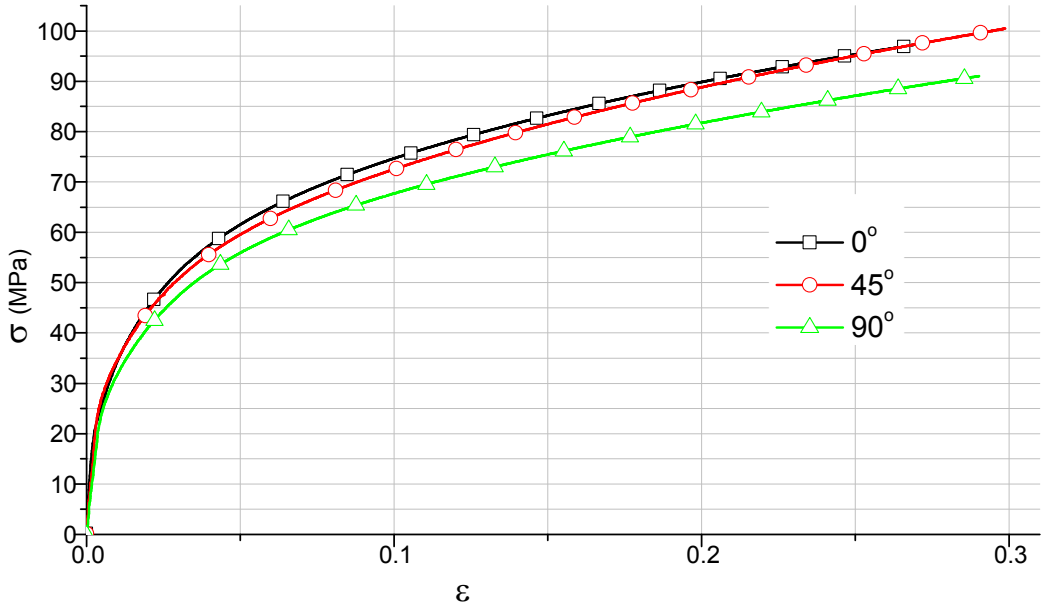

Fig. 28. True stress-strain curve of the initial material at different test angles

Table 3. Yield stress (σ_0), maximum stress (σ_{max}) and uniform strain (ε_u) of the Initial material at different tested angles (θ)

θ (°)	σ_0 (MPa)	σ_{max} (MPa)	ε_u
0	20	97	0.27
45	20	101	0.30
90	20	92	0.28

The changes in thickness during the uniaxial tensile tests are presented in Fig. 29. The results show that the initial material presents higher thickness reduction for θ=45° and lower θ=90°. These differences are better reveled in Fig. 30 and Table 4 where the

anisotropy coefficients for the three investigated directions are presented. The measured R-value is maximum (1.13) and minimum (0.57) for, respectively, θ=90° and θ=45°. These low values of anisotropy coefficients, expressed in a normal anisotropy coefficient ($\overline{R}$) equal to 0.75, are typical for aluminum sheets and contributes to the limited formability of this material (when compared with regular steel grade, which commonly exhibit $\overline{R}$ -values of approximately 2.5 [63]).

Another important parameter that effects the quality of final metallic piece is the planar anisotropy (ΔR) of the sheet. For the material used in this work the measured ΔR-value was 0.35.

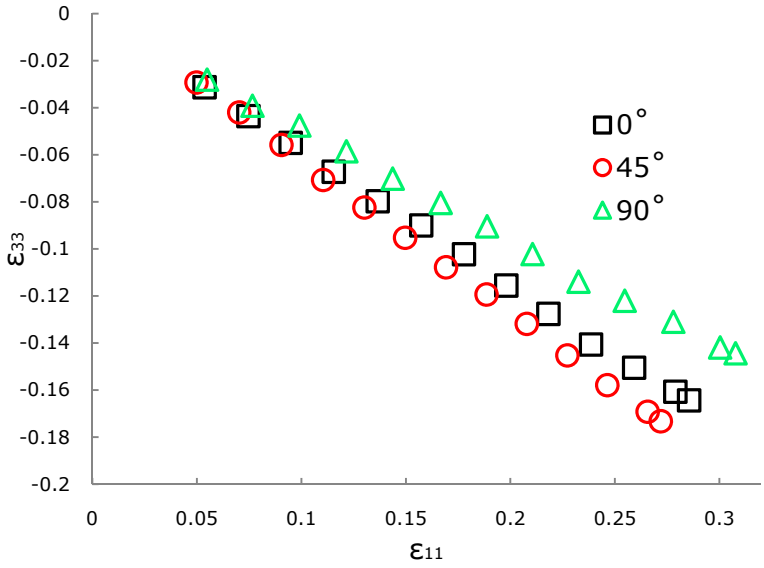

Fig. 29. Thickness (ε_{33}) change with uniaxial strain (ε_{11}) at different tested angles

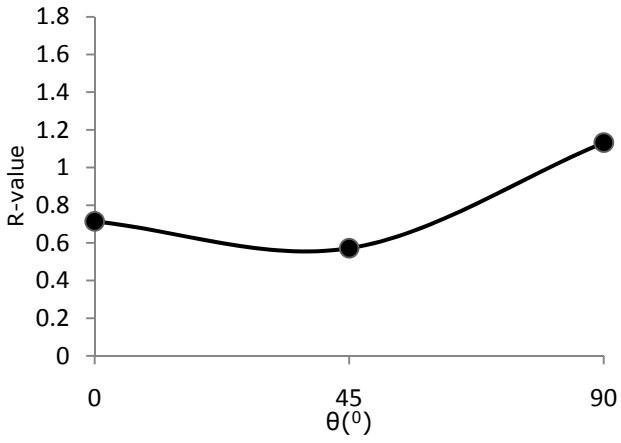

Fig. 30. Anisotropy coefficients of the initial material at different test angles (θ)

Table 4. Anisotropy coefficients of the initial material

θ (°)	R	Normal, $\overline{R}$	Planar, ΔR
0	0.71	0.75	0.35
45	0.57		
90	1.13		

In order to investigate this anisotropic distribution of the strain, {200} and {111} pole figures were acquired for the initial material (Fig. 31). The results show a strong {100} <001> preferential crystallographic orientation of the grains, typical of recrystallized aluminum sheets. The presence of this texture component, known as a cube component, is better identified in Euler space representation (Fig. 32) and commonly associated with low R-values for θ=45° (when compared with the values θ=0° and θ=90°) [10], as observed in the present work.

The transmission electron microscopy (TEM) observations performed on the initial material (Fig. 33) reveal that the grains, of approximately 50 μm size, present very low dislocation density. This is consistent with the measured low yield stress value and, together with the cube texture component detected by X-ray diffraction, allows to conclude that the material was supplied in the recrystallized condition.

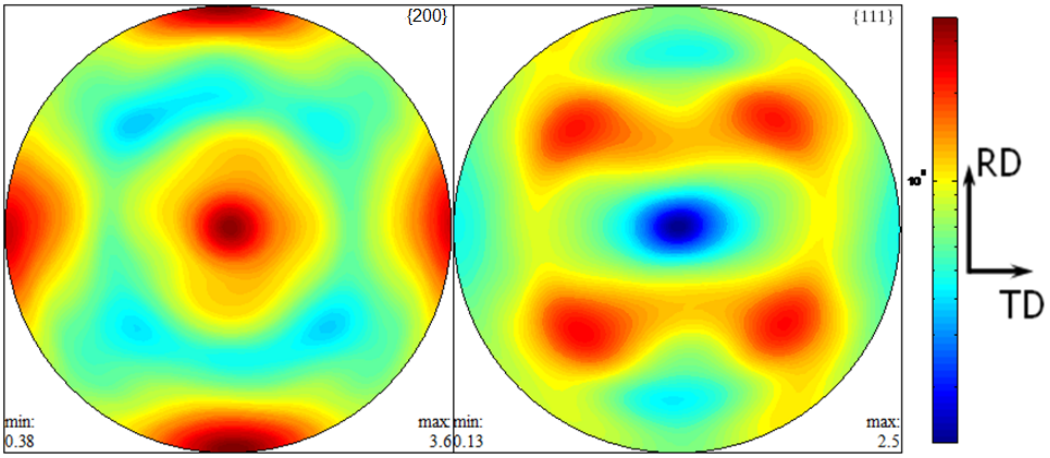

Fig. 31. {200} and {111} pole figures of initial material

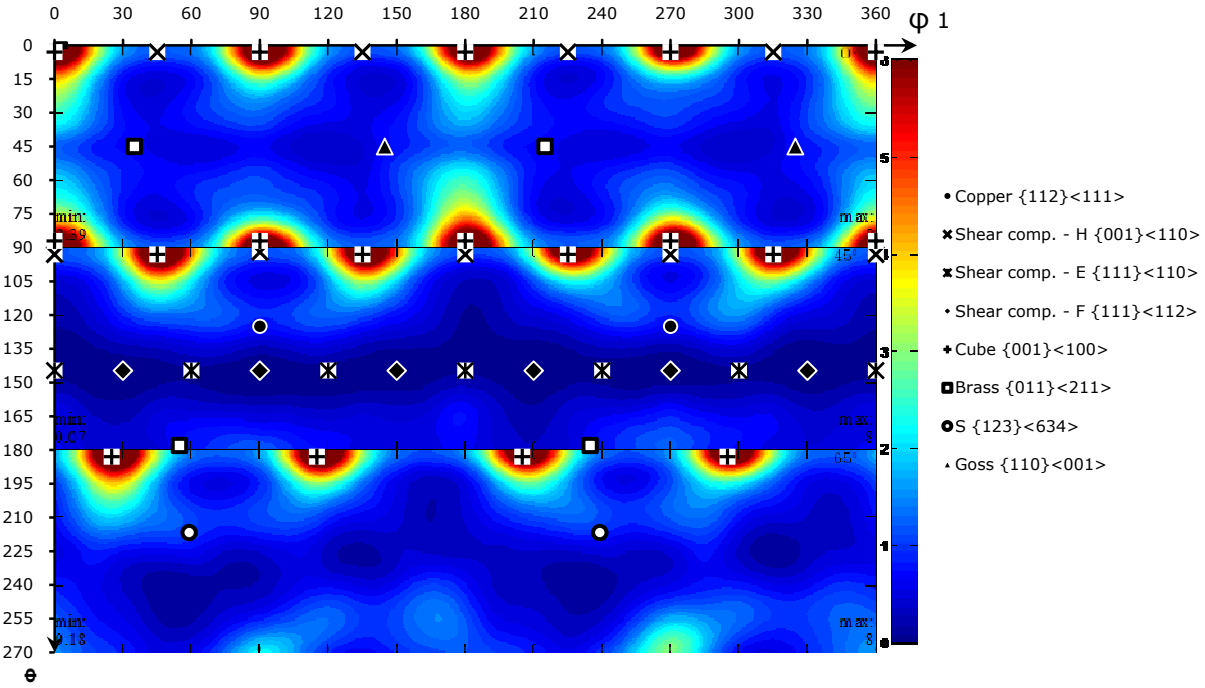

Fig. 32. Crystallographic texture of initial material at φ_2 =0°, 45° and 65° sections of Euler space. The most common ideal FCC texture components are presented

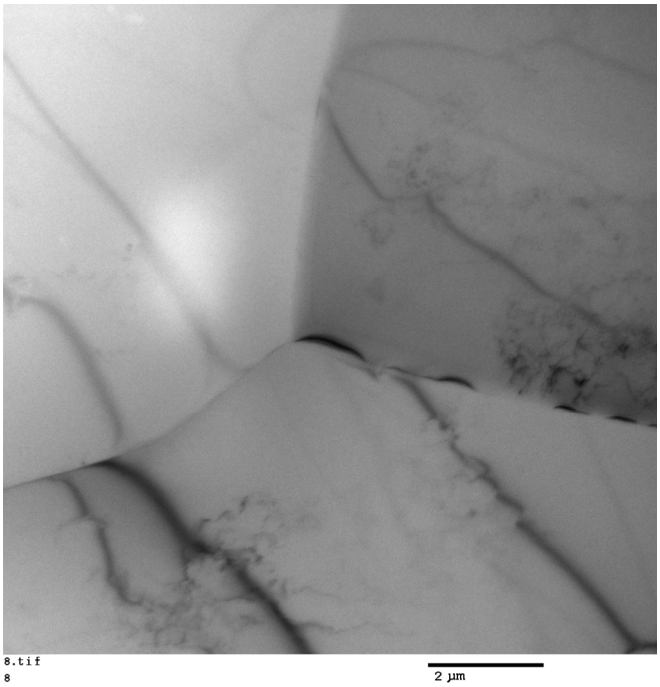

Fig. 33. TEM image of grain boundary triple point in the initial material

4.2Characterization of the material after rolling

When compared with initial material, conventionally and asymmetrically rolled samples show substantial differences in mechanical behavior during tensile test (Fig. 34). Namely, it is observed an increase of yield stress and maximum stress (σ_{max}) together with strong decrease of the uniform plastic deformation, with the total thickness reduction in rolling. After six passes (which correspond to 62% of reduction) the uniform deformation is less than 2% for all samples and the maximum stress increases up to 130-150 MPa (Fig. 35. c), depending on the test angle and rolling type. More specifically, the highest values of σ_{max} were achieved for ASRC and the lowest values for CR samples. These differences can have origin of the dislocation structure or/and crystallographic texture developed during the pre-strain in rolling. To investigate the contribution of each of these physical mechanisms, texture analyses using VPSC model and TEM observations were performed after different rolling types.

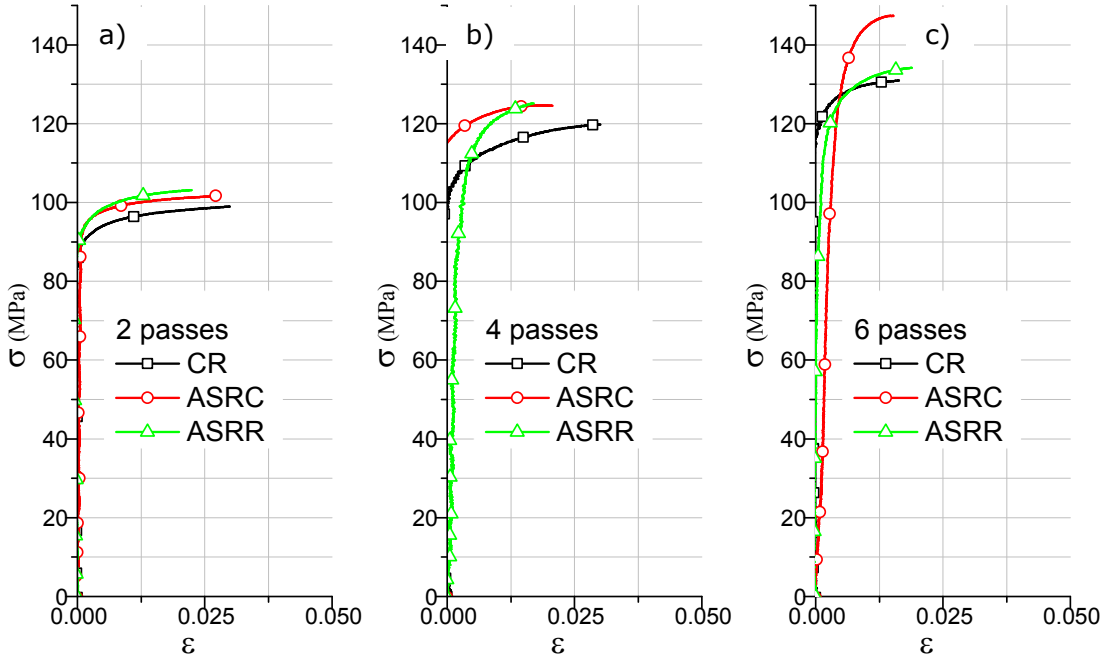

Fig. 34. True tensile stress-strain curves at 0° after a) 2 passes (28% reduction); b) 4 passes (48% reduction) and c) 6 passes (62% reduction)

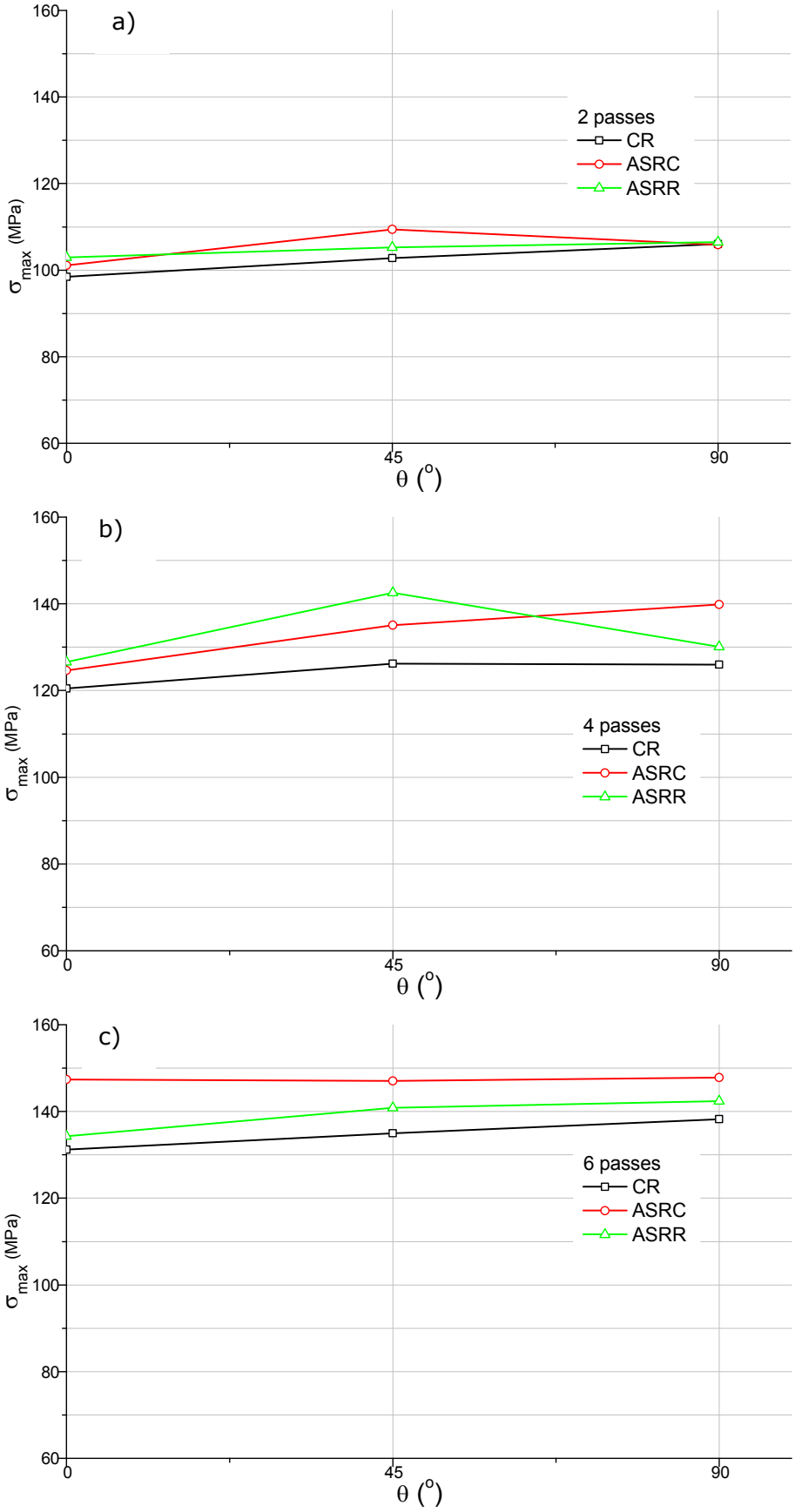

Fig. 35. Maximum stress values at different test angles after: a) 2 passes (28% reduction); b) 4 passes (48% reduction) and c) 6 passes (62% reduction)

In Fig. 36 to Fig. 41 are presented the pole figures and φ_2 =0°, 45° and 65° sections of Euler space of the texture are exhibited in samples after 6 passes using different rolling types. For CR sample, the pole figure presents orthotropic symmetry and is dominated by the typical conventional rolling, Cu, S and (with less intensity) Brass texture components (Fig. 36, Fig. 37). However, different textures are observed in the samples after asymmetric rolling. Namely, for ASRC sample, the pole figure is not orthotropic and only the mirror symmetry along the rolling direction is preserved. Moreover, the rolling component Cu, S and Brass still exist but with different intensities and higher volume fraction of the crystals presents orientations closer from the ideal shear texture components (Fig. 39). The ASRR texture can be regarded as a mixture of CR (Cu, S and Brass, with lower intensity) and initial (cube) texture components (Fig. 41). For both types of asymmetric rolling, the intensity of the ideal shear texture components (E {111} <110>, F {111} <112> and H {001} <110>) are low, even when the macroscopic shear strain imposed to the samples during the pre-strain in ASRC reach the value of $\gamma=0.6$ (Fig. 42).

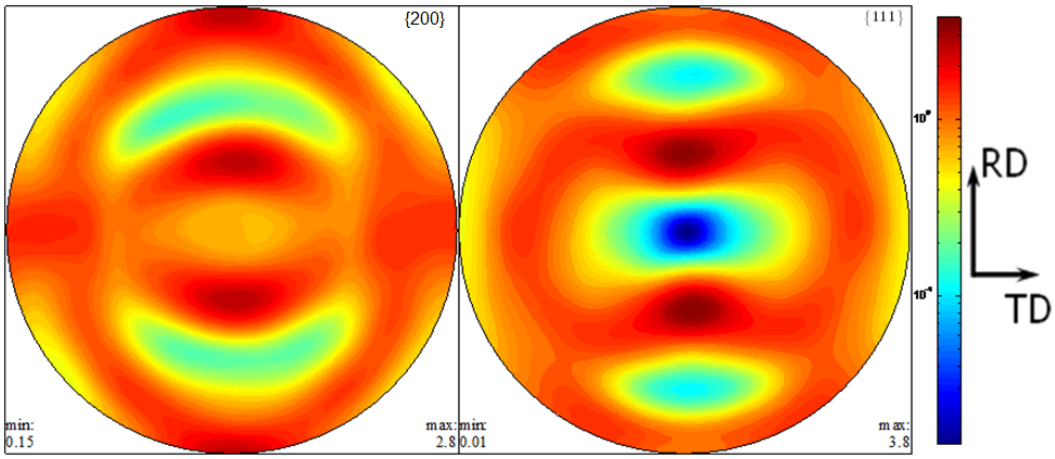

Fig. 36. {200} and {111} pole of CR sample

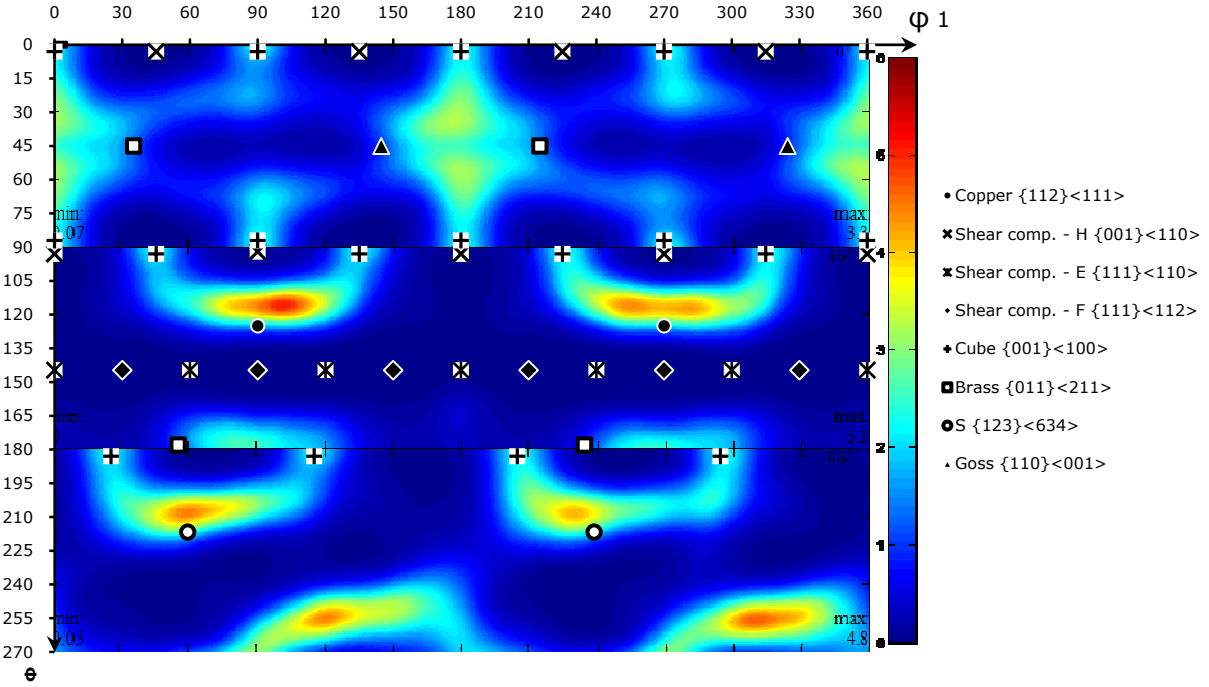

Fig. 37. Crystallographic texture of CR sample at φ_2 =0°, 45° and 65° sections of Euler space. The most common ideal FCC texture components are presented

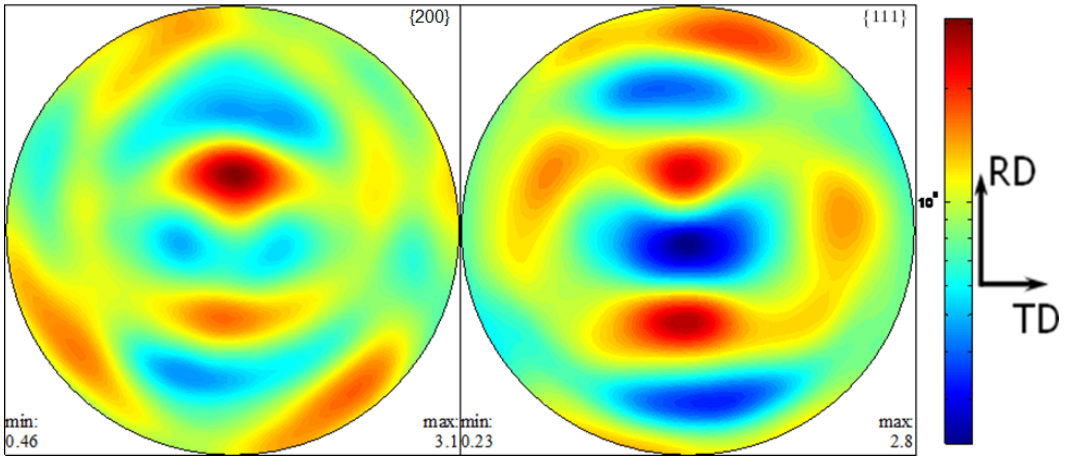

Fig. 38. {200} and {111} pole figures of ASRC sample

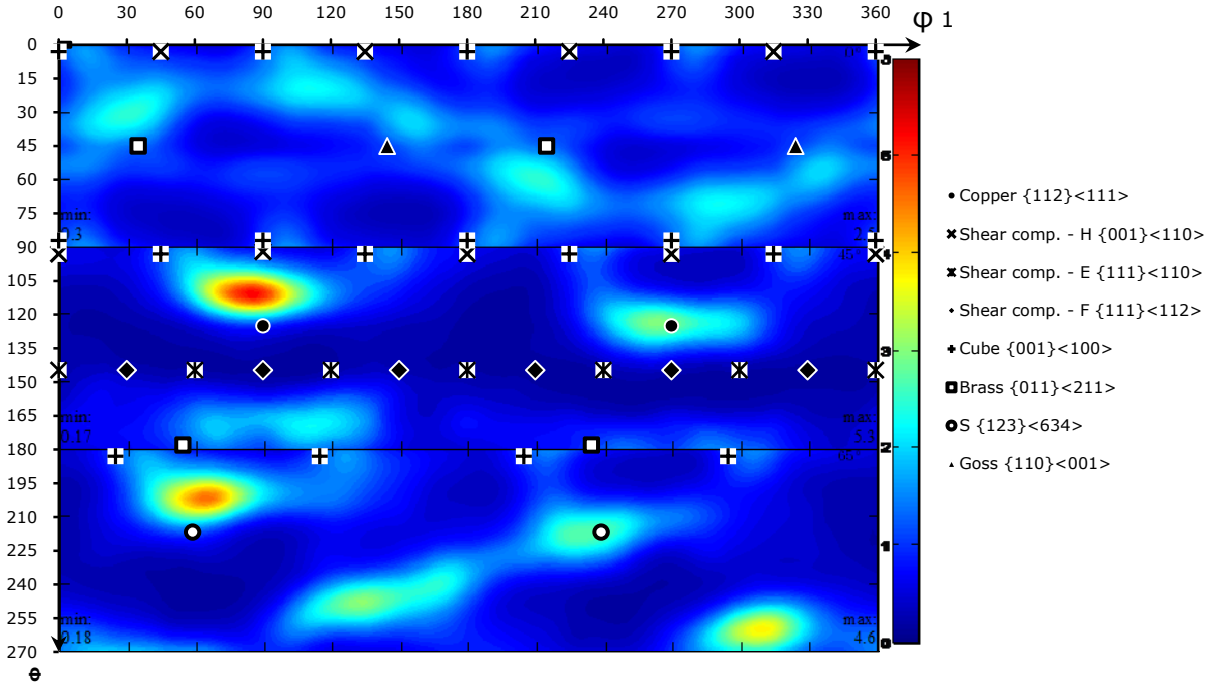

Fig. 39. Crystallographic texture of ASRC sample at φ_2 =0°, 45° and 65° sections of Euler space. The most common ideal FCC texture components are presented

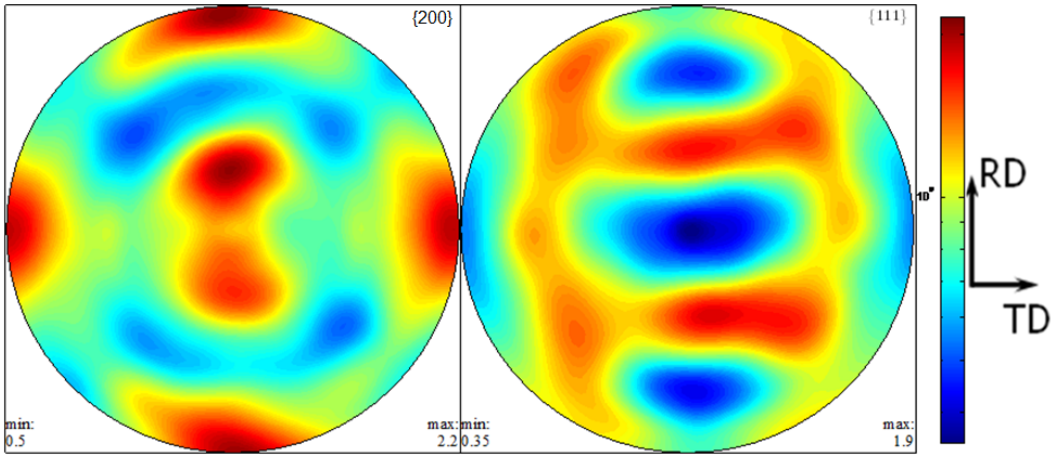

Fig. 40. {200} and {111} pole figures of ASRR sample

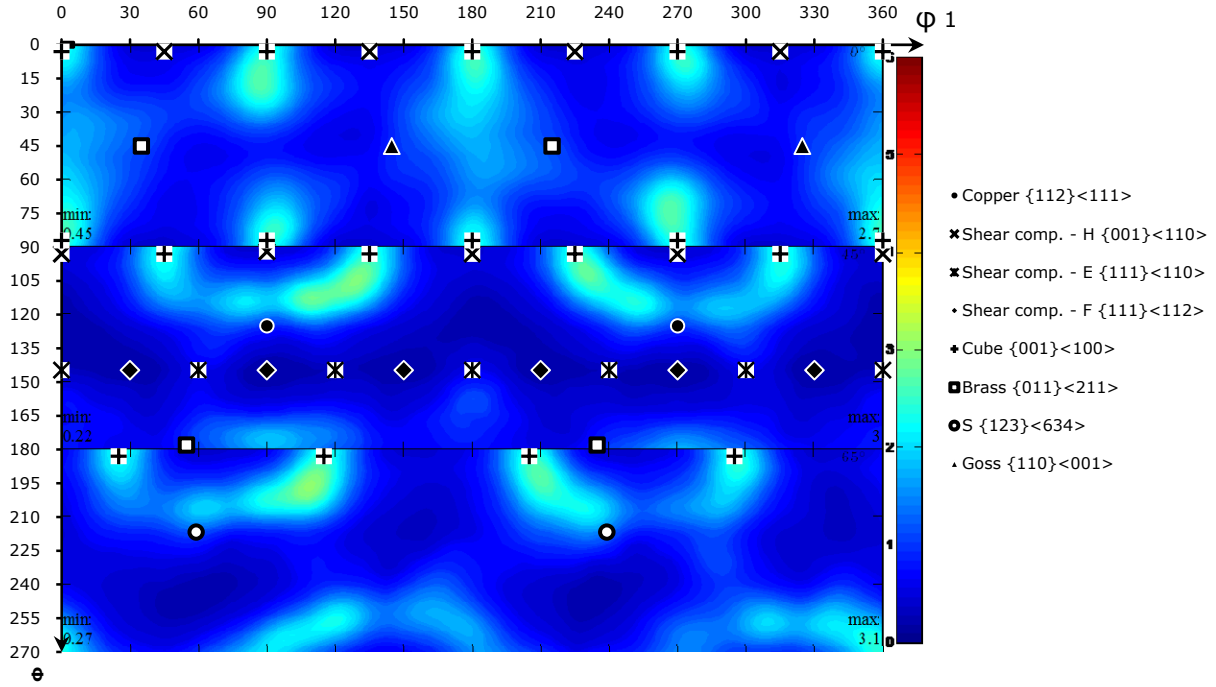

Fig. 41. Crystallographic texture of ASRR sample at φ_2 =0°, 45° and 65° sections of Euler space. The most common ideal FCC texture components are presented

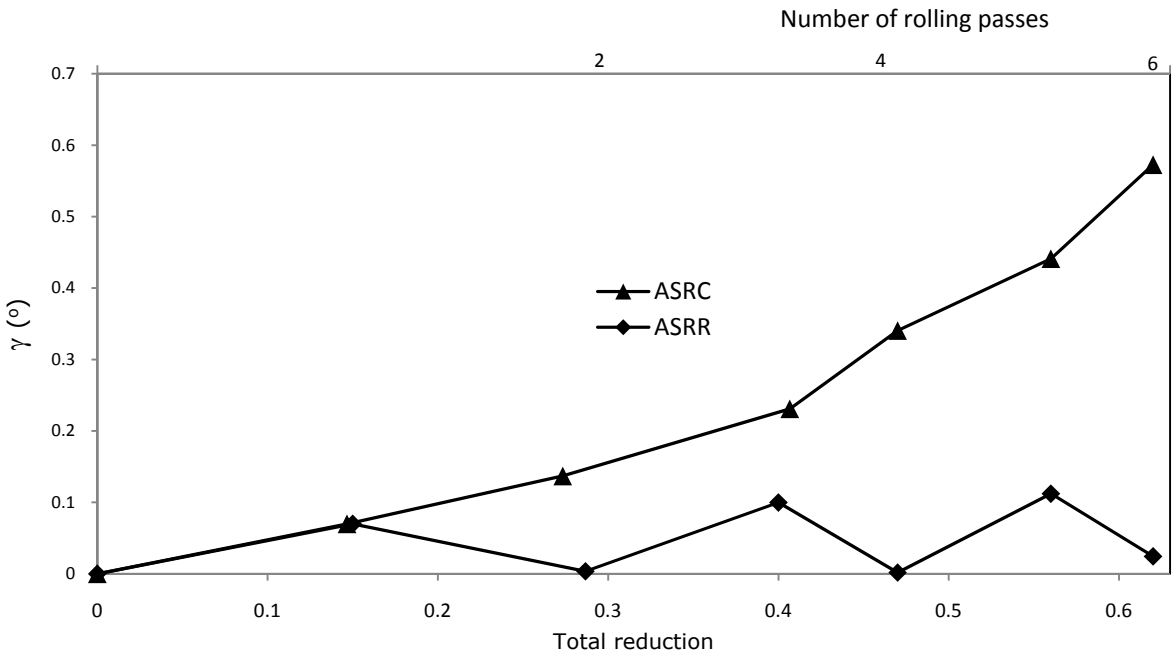

Fig. 42. Variation of macroscopic shear angle (β) and shear strain (γ) with total reduction in asymmetric rolling

The average Taylor factor (<M>) extracted with VPSC model from the experimental crystallographic textures after rolling (Fig. 43) is almost independent of the tensile test direction, except for ASRC samples at θ=0° and 90° (for which <M> is higher).

The effect of these differences which is seen on the $\sigma - \varepsilon$ curves can be calculated using the equation 2.19. Assuming that the influence on the strain of the dislocation structure developed during the pre-strain is independent of the rolling type ($\tilde{\tau}$ does not change with the rolling types) the flow stress is given by:

$$\sigma(\varepsilon,\theta) = \sigma(\varepsilon,\theta)_{ref} \frac{< M(\varepsilon,\theta) >}{< M(\varepsilon,\theta)_{ref} >} \qquad (4.1)$$

where $\sigma(\varepsilon,\theta)_{ref}$ and $< M(\varepsilon,\theta)_{ref} >$ are the experimental flow stress and the calculated <M> for a reference $\sigma - \mathcal{E}$ curve.

Using this expression and selecting the CR $\sigma - \varepsilon$ curve as reference, the effect of the texture on the σ_{max} values is presented in Fig. 44. For comparison, in the same figure are also shown the measured σ_{max} values.

These results show that the predicted σ_{max} values for asymmetrically rolled samples are always lower than the experimental measured ones. This proves that the differences in crystallographic orientation of the grains after different rolling types has influence on the reloading flow stress (for θ=0° and 90°) but cannot explain the changes of experimental σ_{max} value with the rolling type. Indeed, the difference in experimental σ_{max} values after asymmetric and conventional rolling should be the result of two contributions: differences in crystallographic texture and in dislocation microstructure.

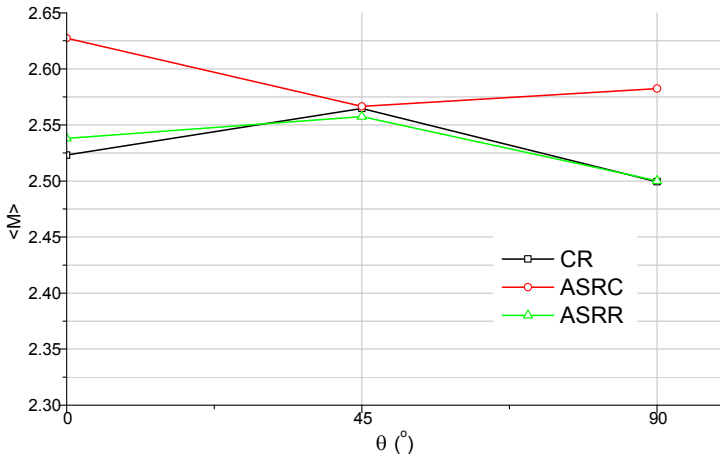

Fig. 43. <M> value for different rolling types and tensile test angles (after 6 passes)

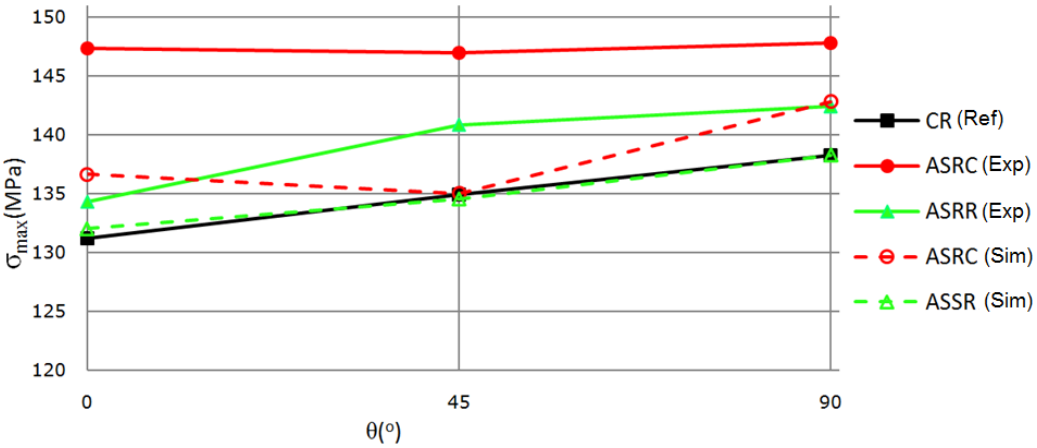

Fig. 44. Experimental (Exp) and simulated (Sim) σ_{max} values for different rolling types and test angle (after 6 passes). The CR curves were used as reference (Ref) in the simulations

In Fig. 45, Fig. 46 and Fig. 47 are presented the TEM observations for CR, ASRC and ASRR samples. The dislocation structure in all samples is characterized by the presence of equiaxial dislocation cells (typical in rolled samples, due to activation of the large number

of slip systems) with around 1-2 μm size, with many dislocations inside and relatively large crystallographic misorientations. From the comparison between these figures it is not possible to detect significant differences between dislocation microstructures that could explain the differences in σ_{max} presented by the samples after different rolling types.

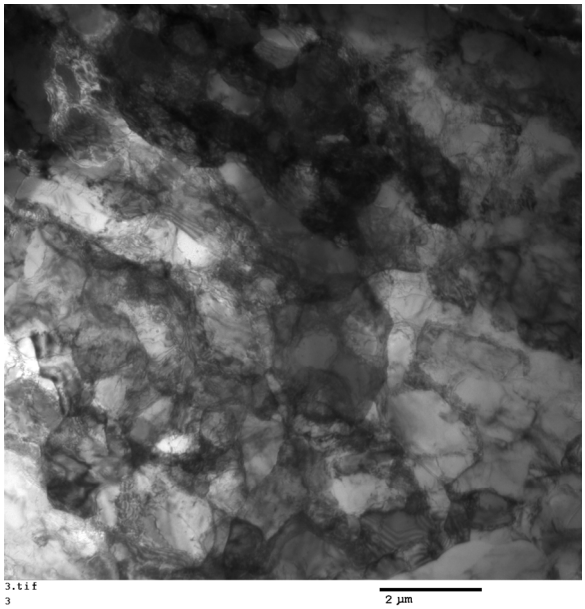

Fig. 45. TEM image of the dislocation microstructure developed in the CR sample, after 6 passes

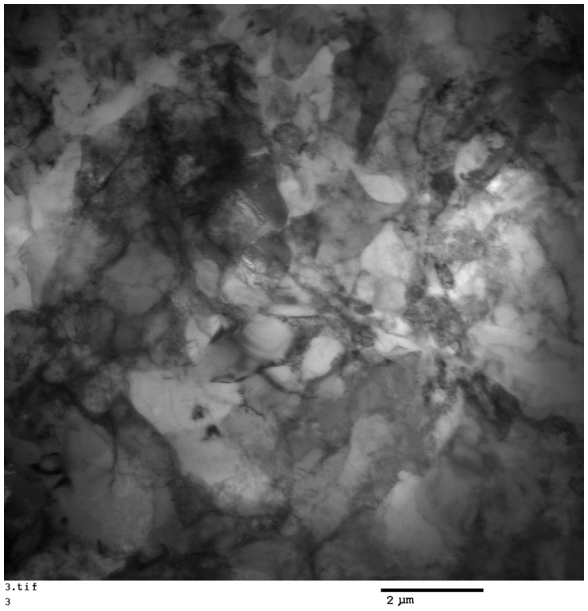

Fig. 46. TEM image of the dislocation microstructure developed in the ASRC sample, after 6 passes

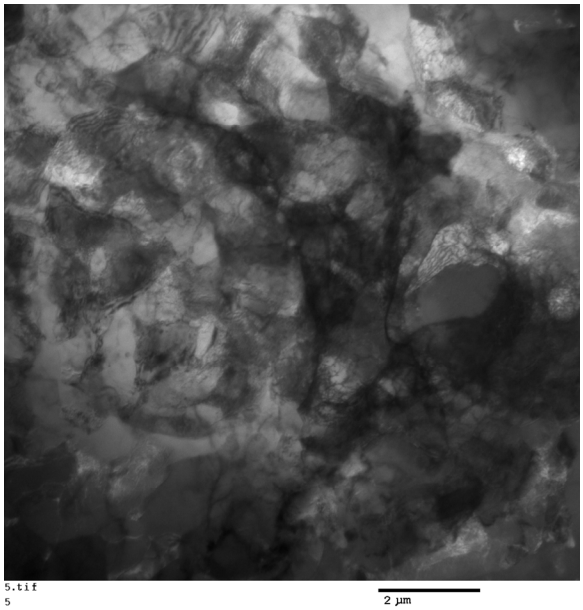

Fig. 47. TEM image of the dislocation microstructure developed in the ASRR sample, after 6 passes

Due to the additional shear strain imposed during the asymmetric rolling, the change of the strain path in reloading (characterized by the α parameter, which calculation is presented in Appendix) is different for CR and ASRC (Fig. 48). However, the differences in this parameter are small (reflecting relatively low γ values imposed during ASRC) and cannot explain the observed differences in σ_{max} values. Therefore, other factors must be considered to explain these differences such as, changes in cell size and shape along the thickness and/or in crystallographic misorientation between neighbor cells. The sample preparation for the dislocation microstructure analyses in the perpendicular plane of the sheet is difficult due to the small thickness of the rolled samples (around 1mm) and the misorientation is complex to measure (requiring a point-to-point crystallographic orientation mapping) and compute its influence on the mechanical behavior of the sample.

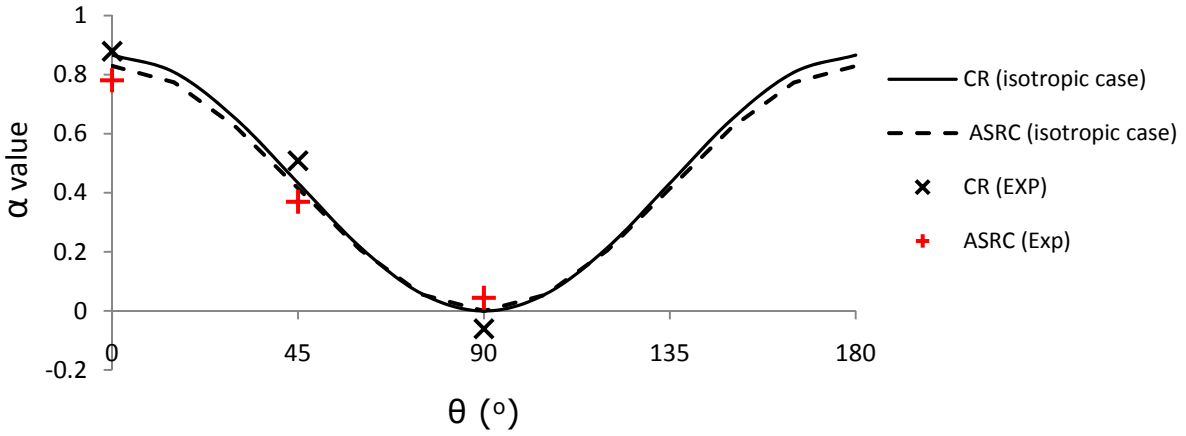

Fig. 48. α value for CR and ASRC (after 6 passes) using experimental R values and R=1 (isotropic cases)

Despite the need of additional studies to explain completely the differences in σ_{max}, the performed tensile tests show that the pre-deformation strongly reduces the uniform plastic strain (ε_u) of the sample during the reloading and limits the study of the material formability after rolling. This limitation can be overcome by recovering the pre-deformation dislocation structure through an annealing after rolling.

4.3 Heat treatment

In order to keep the textures developed during the rolling, the selected heat treatment conditions should promote dislocation annihilation without recrystallization. To find these conditions a set of CR specimens after 6 passes was heat treated at different temperatures and dwell times.

The uniaxial tensile $\sigma-\varepsilon$ exhibited by the heat treated samples (Fig. 42 and Table 5) show that, with increase of temperature and/or time, the yield and maximum stresses decrease and the uniform plastic deformation increases.

The samples annealed at 270° C for 1h and at 260° for 2h show similar mechanical behaviors: relatively high stress levels, but still low uniform deformation (around 5-6%). After heat treatment at 310° during 1h, the material presents a $\sigma-\varepsilon$ curve similar to the initial recrystallized material.

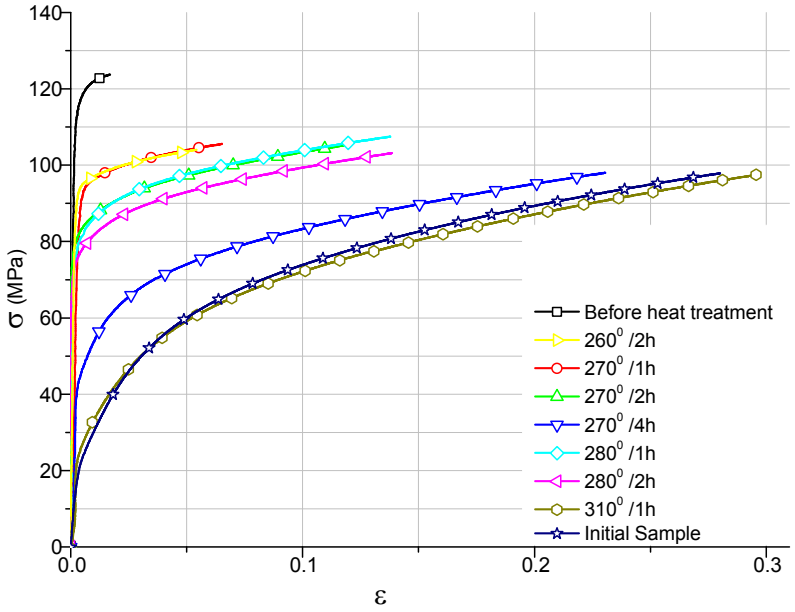

Fig. 49. Tensile true stress-strain curves of CR samples after different annealing conditions (θ=0°)

Table 5. Yield stress (σ_0), maximum stress (σ_{max}) and uniform strain (ε_u) of CR samples after heat treatment in different conditions

T (C°)	Dwell (min)	σ_0 (MPa)	σ_{max} (MPa)	ε_u
260	120	92	105	0.06
270	60	92	107	0.07
270	120	79	105	0.13
270	240	40	98	0.23
280	60	78	114	0.14
280	120	77	102	0.14
310	60	20	98	0.27

At 270° C for 2h and at 280° C for 1h the samples show similar mechanical behavior with relatively high yield strength (about 80 MPa) and the moderate uniform strain (around 0.15). It was decided to select the condition with lower dwell time (280°C during 1h) to heat treated the rolled samples.

The effect of selected annealing conditions on the crystallographic texture and dislocation microstructure is presented in Fig. 50 and Fig. 51. The comparison of Fig. 50 and Fig. 36 shows that the crystallographic texture after heat treatment is preserved. Moreover, from Fig. 51 and Fig. 45 can be confirmed that the microstructure is defined by sub-grain structure with 1-2 μm size and low dislocation concentration inside. The mentioned above

allows to conclude that the selected heat treatment conditions (280^{o} and 1h) promote the recovery of the samples without significant changes in the texture.

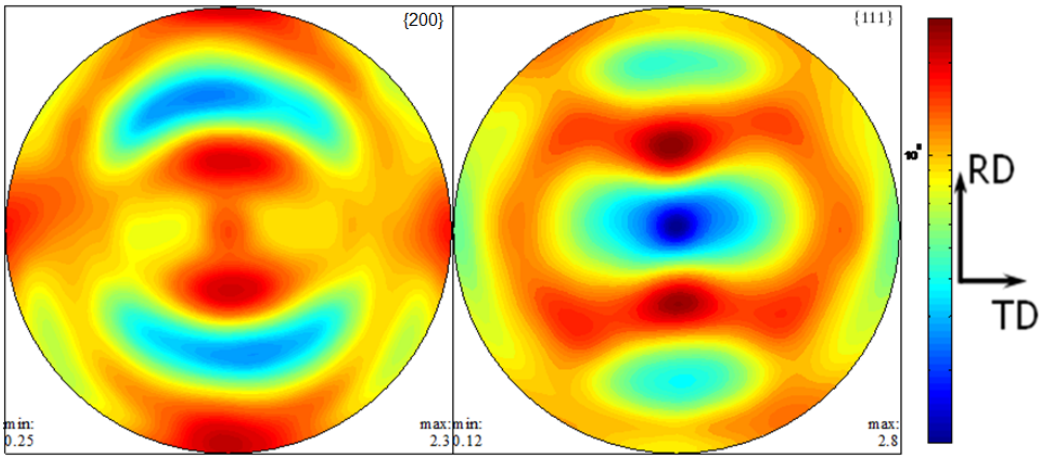

Fig. 50. {200} and {111} pole figures of CR sample after heat treatment at 280^{o} for 1h

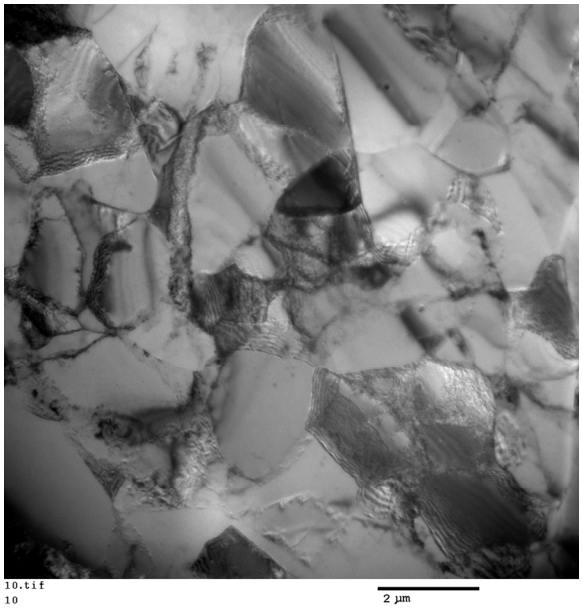

Fig. 51. TEM images of the microstructure developed in the CR sample after heat treatment at 280^{o}C for 1h

4.4Characterization of the material after rolling and heat treatment

The mechanical behavior during the tensile test after rolling and heat treatment is presented in Fig. 52, Fig. 53 and Fig. 54. For three investigated orientations, higher values of flow stress before necking (which occurs at lower strains compare to asymmetric rolled samples) are observed for conventional rolled samples. Moreover, the ASRC and ASRR samples present similar $\sigma-\varepsilon$ curves but different uniform strain values (Table 6, Table 7 and Table 8).

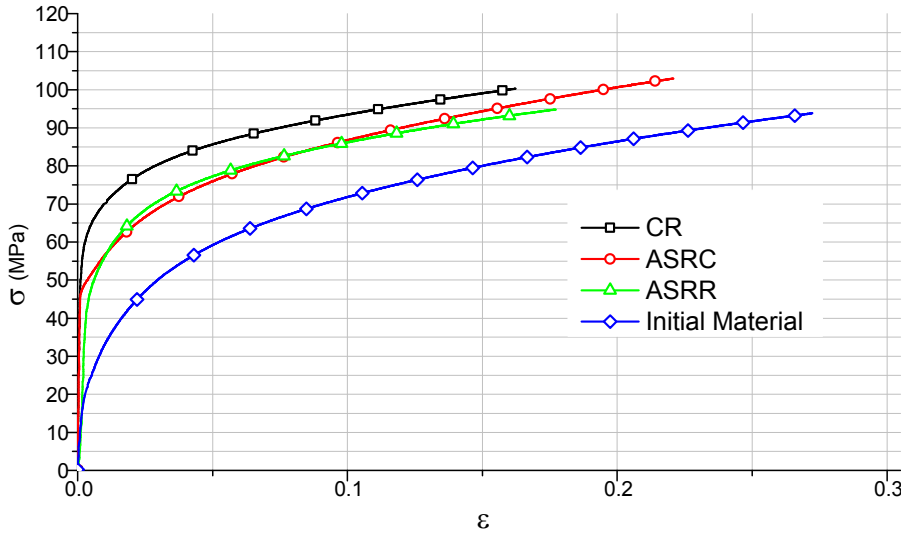

Fig. 52 Tensile true stress-strain curves at 0° of rolled and heat treated samples

Table 6. Yield stress (σ_0), maximum stress (σ_{max}) and uniform deformation (ε_u) at 0° of rolled and heat treated samples

Rolling	σ_0 (MPa)	σ_{max} (MPa)	ε_u
CR	55	100	0.16
ASRC	43	103	0.22
ASRR	45	95	0.18

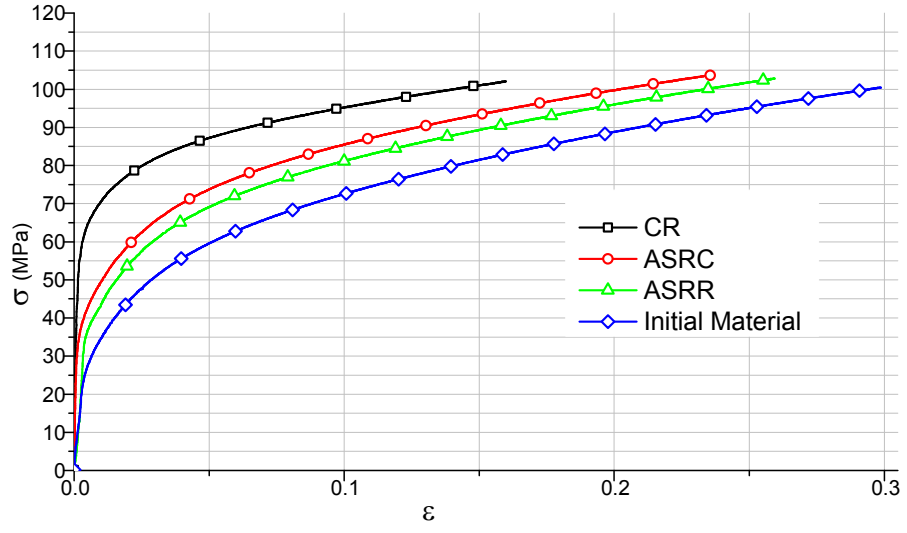

Fig. 53 Tensile true stress-strain curves at 45° of rolled and heat treated samples

Table 7. Yield stress (σ_0), maximum stress (σ_{max}) and uniform deformation (ε_u) at 45° of rolled and heat treated samples

Rolling	σ_0 (MPa)	σ_{max} (MPa)	ε_u
CR	55	102	0.16
ASRC	40	104	0.23
ASRR	38	103	0.26

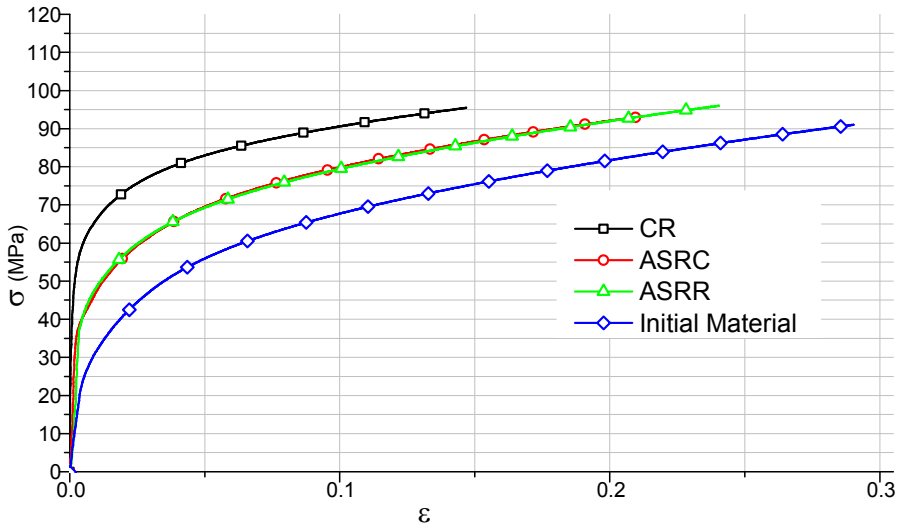

Fig. 54 Tensile true stress-strain curves at 90° of rolled and heat treated samples

Table 8. Yield stress (σ_0), maximum stress (σ_{max}) and uniform deformation (ε_u) at 90° of rolled and heat treated samples

Rolling	σ_0 (MPa)	σ_{max} (MPa)	ε_u
CR	50	95	0.15
ASRC	35	93	0.21
ASRR	35	95	0.24

Differences in the distribution of the strain along the length, width and thickness were also observed during the tensile test (Fig. 55 and Table 9). Namely, the CR samples present highest average thickness reduction. The most favorable anisotropic strain behavior (the highest normal $\overline{R}$ and the lowest planar ΔR values) was presented by ASRC samples. More specifically, an increase of 34% and 57% was observed in the normal anisotropy coefficient ($\overline{R}$) value for ASRC, when compared with CR and initial material, respectively. The improvement, but with a lower magnitude, of $\overline{R}$ was also measured for ASRR samples (10% and 29%). The planar anisotropy coefficient (ΔR) after ASRC was -0.12, which

corresponds to a decrease in the absolute value of ΔR of 68% and 66%, respectively. An increase of this parameter was observed for ASRR (30% and 40%).

These results show that asymmetric rolling (in particular ASRC) can be used to improve the anisotropic behavior of aluminum sheets through the change of crystallographic orientation of the grains.

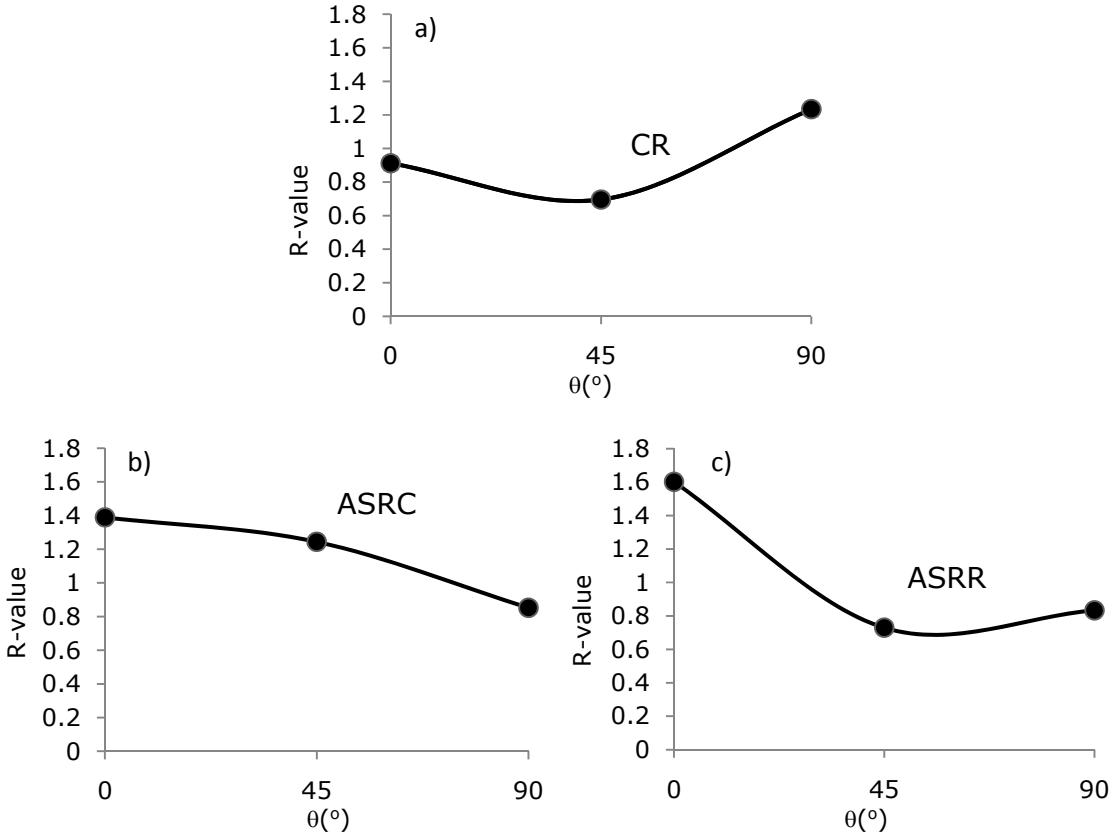

Fig. 55. Anisotropy coefficient of rolled and heat treated samples a) CR; b) ASRC; and c) ASRR

Table 9. Anisotropy coefficient of rolled and heat treated samples

Specimen	θ( )	R	Normal ($\overline{R}$)	Planar (ΔR)
CR	0	0.91	0.88	0.38
	45	0.70		
	90	1.23		
ASRC	0	1.39	1.18	-0.12
	45	1.24		
	90	0.85		
ASRR	0	1.60	0.97	0.49
	45	0.73		
	90	0.83		

Another important difference showed by $\sigma-\varepsilon$ curves is the strain hardening evolution during the tensile test. Indeed, all rolled samples present a higher flow stress values (for the same strain amount) than the initial material. However, due to a reduction of the ε_u for all orientations and rolling types, this increase of flow stress did not result in any significant increase of $\sigma_{\max}$.

The influence of crystallographic texture for these strain hardening differences was investigated (as in the section 4.2) analyzing the $\sigma-\varepsilon$ curves simulated using the equation (4.1) and <M> values extracted from pole figures measured for rolled and heat treated samples (Fig. 56). The results from these calculations (Fig. 57) show that the differences in the initial crystal orientations after CR, ASRC and ASRR have almost no influence on the flow stress and cannot explain the observed differences.

The quality of the results computed with the VPSC model was evaluated for $\theta=0^{o}$ using two methods: comparing the <M> values (Fig. 56.a) calculated from the experimental textures before (continues lines) and after (dashed lines) the tensile tests; and comparing the pole figures simulated with the model, and the texture measured after tensile test at 0^{o} (Fig. 58 to Fig. 60). For both methods a good agreement is observed, showing that VPSC model can be used to analyze the influence of crystallographic texture on $\sigma-\varepsilon$ curves.

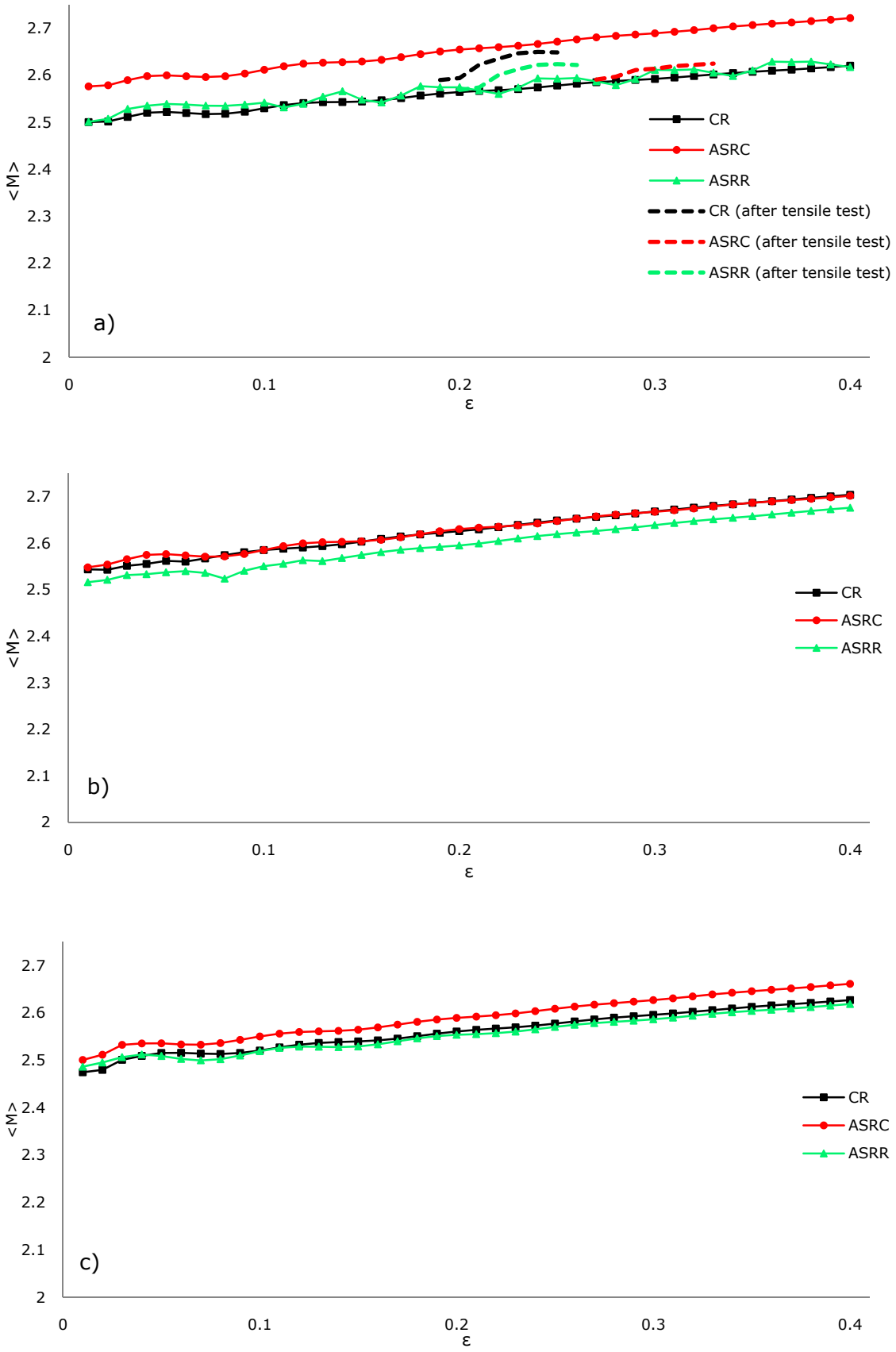

Fig. 56. Evolution of <M> during tensile test at a) 0°; b) 45° and c) 90° of rolled and heat treated samples. Continuous lines - values calculated before tensile test; dashed lines - values calculated from pole figures after tensile test

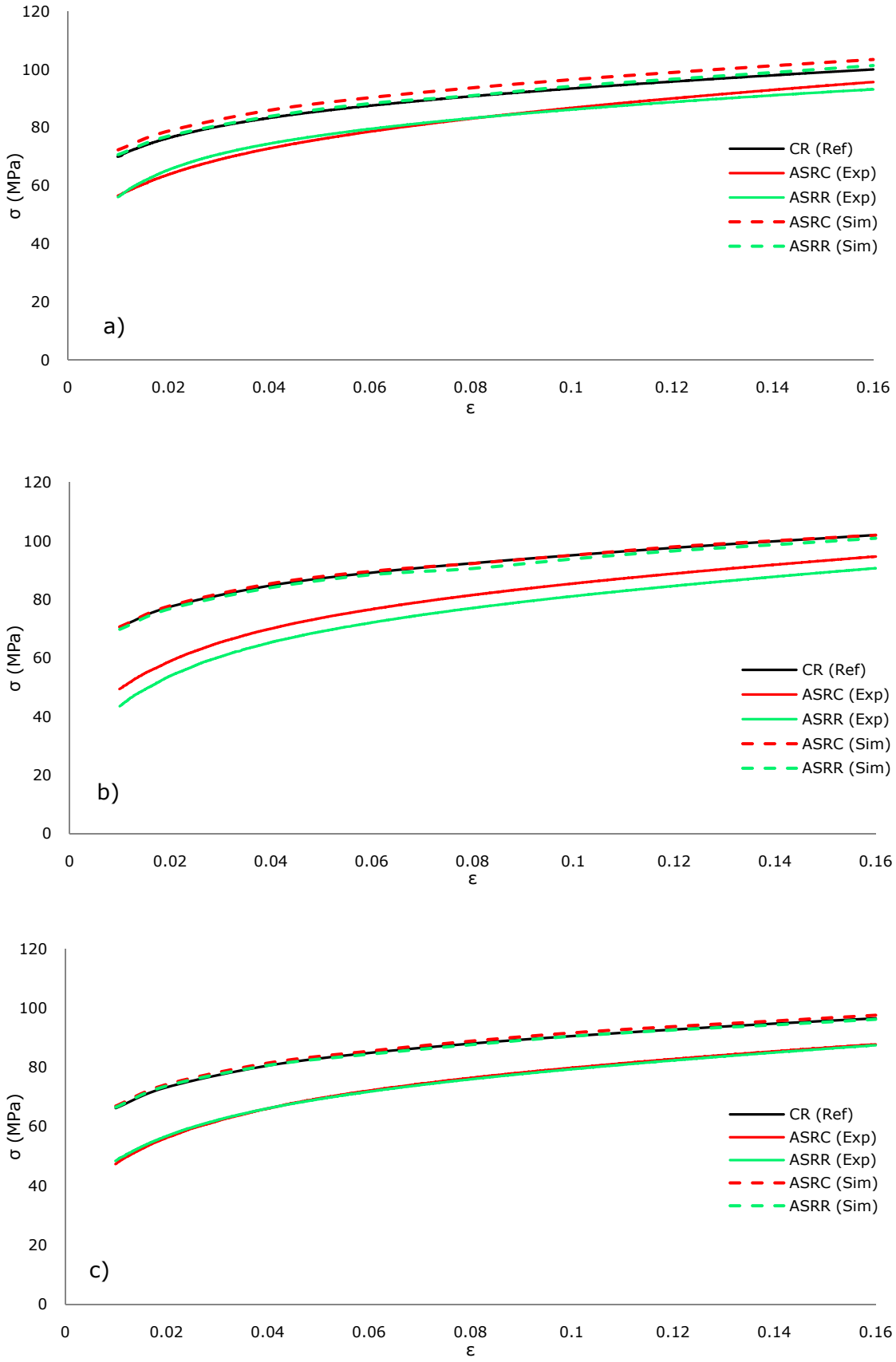

Fig. 57. Experimental (Exp) and simulated (Sim) true stress-strain curves at a) 0°, b) 45° and c) 90° for rolled and heat treated samples. The CR curves were used as reference (Ref) in the simulations

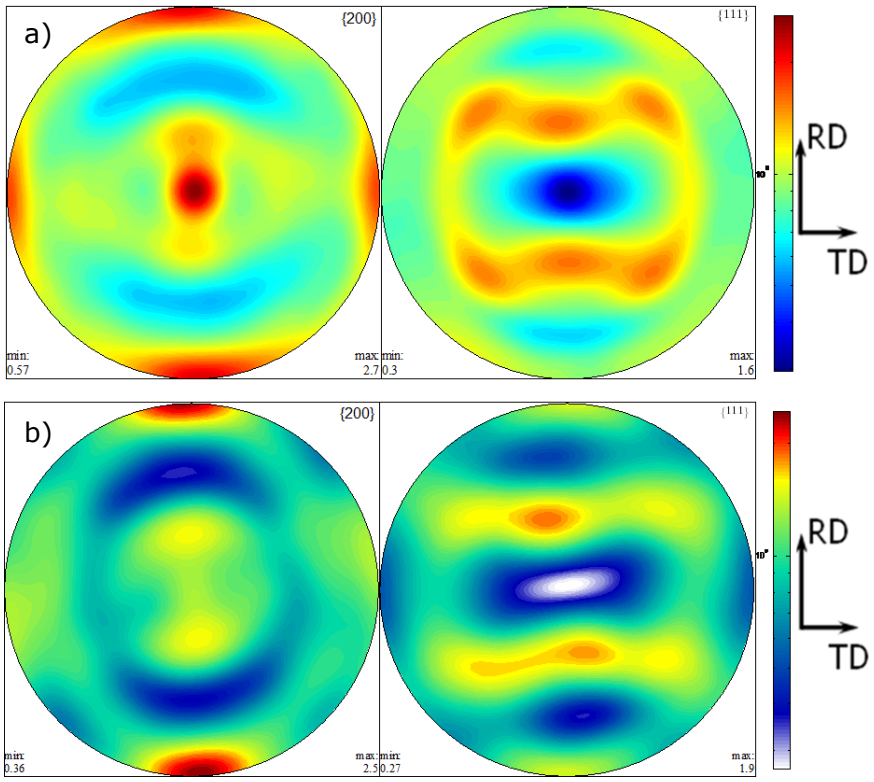

Fig. 58. Experimental (a) and simulated (b) {200} and {111} pole figures for CR and annealed sample after tensile test at 0°

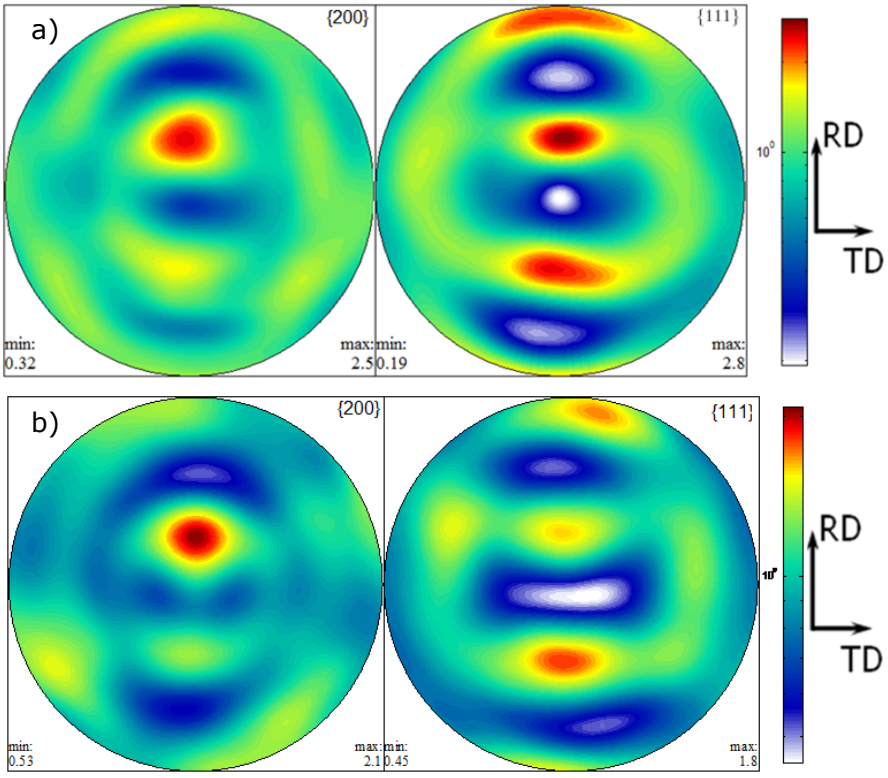

Fig. 59. Experimental (a) and simulated (b) {200} and {111} pole figures for ASRC and annealed sample after tensile test at 0°

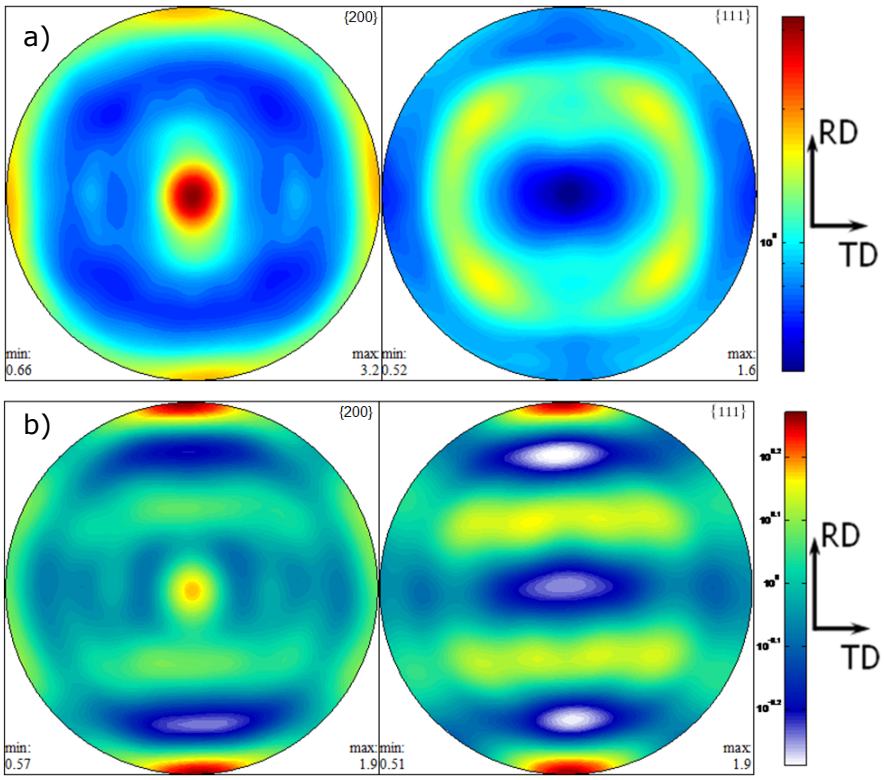

Fig. 60. Experimental (a) and simulated (b) {200} and {111} pole figures for ASRR and annealed sample after tensile test at 0°

The exclusion of the texture effect to explain the difference in the flow stress after rolling and heat treatment reveals that these differences should have microstructural origin. However the TEM observations performed on the sheet plane before tensile test (Fig. 61) show similar microstructures defined by sub-grains with 1-2μm size and cannot explain the strain hardening differences presented by CR, ASRC and ASRR samples at the beginning of the reloading.

Moreover, the TEM observations performed after tensile tests (Fig. 62) did not show also any microstructural feature that could explain the differences between $\sigma-\varepsilon$ curves for higher strain values. Additional microstructural analysis (which includes microstructural characterization in the thickness plane and measurements of sub grains misorientation, as proposed in section 4.2) should be preformed to explain completely the strain hardening differences presented by CR, ASRC and ASRR samples.

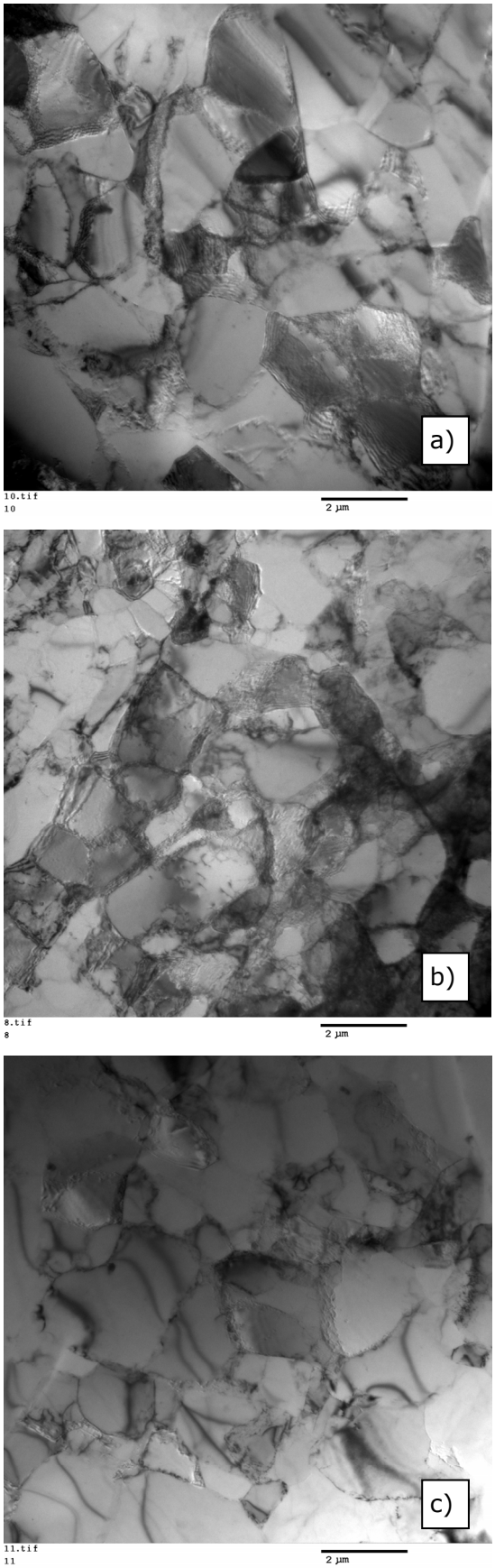

Fig. 61. TEM images of CR (a), ASRC (b) and ASRR (c) samples after heat treatment

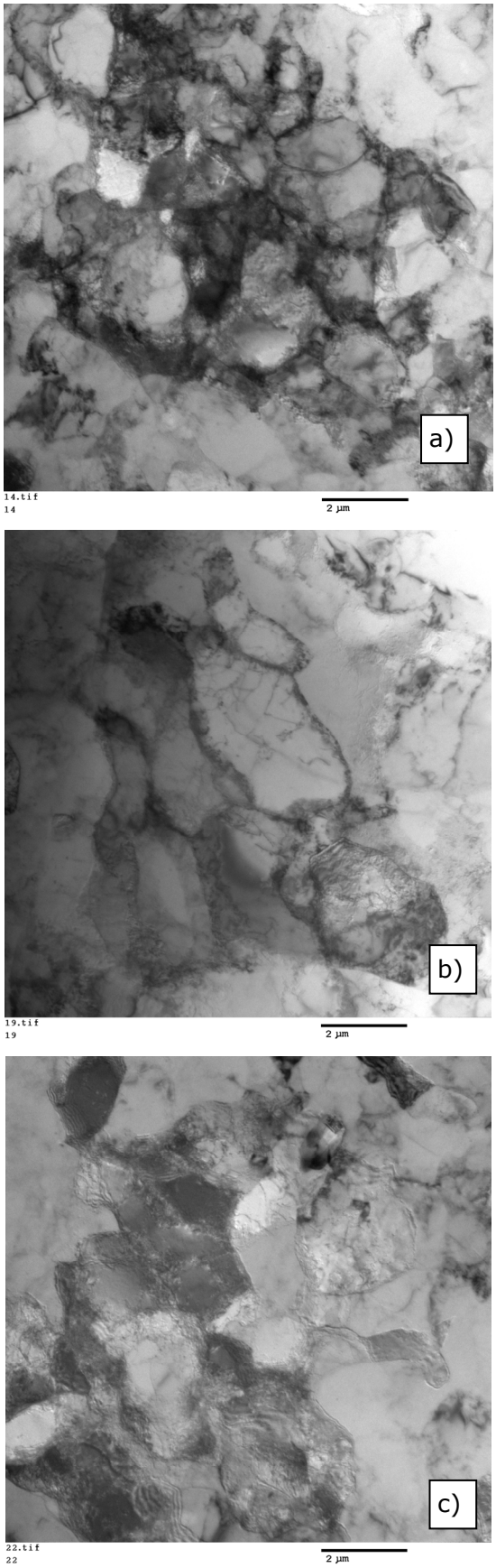

Fig. 62. TEM images of microstructure of CR (a), ASRC (b) and ASRR (c) heat treated samples after tensile test at 0°. All the observations were performed for $\mathcal{E}=\mathcal{E}_u$.

5 Conclusions

The asymmetric rolling of 1050 aluminum sheets was investigated. Three different types of rolling were studied: conventional rolling (CR), asymmetric rolling continues (ASRC) and asymmetric rolling reverse (ASRR). The influence of crystallographic orientation of the grains and the dislocation structure developed during the plastic deformation on the mechanical behavior of the material during the uniaxial tensile test were analyzed using X-ray diffraction and transmission electron microscopy. The visco-plastic self consistent (VPSC) model was used to quantify the effect of crystallographic texture on the stress-strain curves obtained by tensile tests performed on the rolled samples before and after the heat treatment.

From the results obtained the following conclusions can be drawn:

1. With the increase of total thickness reduction, the maximum tensile strength (σ_{max}) increases and the uniform strain (ε_u) decreases. After 6 passes (62% of reduction) the uniform deformation was less than 2%. For all the investigated reduction values (28%, 48% and 62%), the asymmetric rolled samples have presented the higher values of σ_{max} than the conventional rolled ones.
2. The texture analyses have shown, for asymmetrically rolled samples, the presence of crystals with orientation near to the ideal shear texture components. However, the intensities of these components were relatively low in both ASRC and ASRR samples.
3. The conditions used for annealing (280°C and 1h) did not promote recrystallization and the crystallographic texture developed during different types of rolling was preserved. After this heat treatment the microstructure was characterized by the presence of sub-grains with 1-2μm size.
4. After the heat treatment, the asymmetric rolled samples showed an increase of normal anisotropy coefficient, when compared to the conventional rolled or initial material. For ASRC, a decrease of planar anisotropy coefficient was observed. These results show that asymmetric rolling can be used to improve the formability of 1050 aluminum alloy sheets.
5. The selected rolling and heat treatment conditions allowed to produce a grain refined microstructures. However, the effect on the flow stress of this grain refinement was more intense for conventionally rolled samples than for asymmetrically processed ones.

6 Proposals for future work

Based on the results achieved, the following is proposed for future work:

- In order to increase the amount of shear texture components by asymmetric rolling, different rolling parameters should be studied, such as different rolls speed ratios, reduction per pass, friction, etc.
- Additional microstructural analyses (which should include microstructural observations in the thickness plane of the sheet and measurements of cells/sub-grains misorientation) ought to be performed to explain the differences in the tensile flow stresses observed after the CR, ASRC and ASRR.

References

[1] Dieter G.E. (2003). Handbook of Workability and Process Design, IBSN 0-87170-778-0, ASM International.

[2] Avitzur, B. (1983). Handbook of Metal-Forming Processes, ISBN 0-471-03474-6, Wiley-Interscience Publication, New York.

[3] Dieter, G. E. (1988). Mechanical Metallurgy SI Metric Edition, McGraw-Hill Book Co.

[4] Salimi, M. and F. Sassani (2002). "Modified slab analysis of asymmetrical plate rolling." International Journal of Mechanical Sciences 44(9): 1999-2023.

[5] Gudur, P. P., M. A. Salunkhe, et al. (2008). "A theoretical study on the application of asymmetric rolling for the estimation of friction." International Journal of Mechanical Sciences 50(2): 315-327.

[6] Hwang, Y.-M. and G.-Y. Tzou (1997). "Analytical and experimental study on asymmetrical sheet rolling." International Journal of Mech. Sciences 39(3): 289-303.

[7] Tzou, G.-Y. (1998). "Relationship between frictional coefficient and frictional factor in asymmetrical sheet rolling." Journal of Materials Processing Technology 86(1-3): 271-277.

[8] Kim, K. H. and D. N. Lee (2001). "Analysis of deformation textures of asymmetrically rolled aluminum sheets." Acta Materialia 49(13): 2583-2595.

[9] Lee, J.-K. and D. N. Lee (2008). "Texture control and grain refinement of AA1050 Al alloy sheets by asymmetric rolling." International Journal of Mechanical Sciences 50(5): 869-887.

[10] Lopes, A. L. B. (2001). Análise microestrutural das instabilidades plásticas em materiais metálicos, Aveiro. PhD: 227.

[11] Simões, F., R. de Sousa, et al. (2009). "Effect of asymmetrical rolling and annealing the mechanical response of an 1050-o sheet." International Journal of Material Forming 2(0): 891-894.

[12] Karaman, I., H. Sehitoglu, et al. (2000). "Modeling the deformation behavior of Hadfield steel single and polycrystals due to twinning and slip." Acta Materialia 48(9): 2031-2047.

[13] Schmid E. (1924), Proc. Int. Congr. Appl. Mech. (Delft) 342.

[14] Sestak B., (1979) Proc. 5th Int. Conf. On the Strength of Metals and Alloys, Aachen, Germany, p. 1461.

[15] Kocks, U. F. and H. Mecking (2003). "Physics and phenomenology of strain hardening: the FCC case." Progress in Materials Science 48(3): 171-273.

[16] Austin, R. A. and D. L. McDowell (2010). "A dislocation-based constitutive model for viscoplastic deformation of FCC metals at very high strain rates." International Journal of Plasticity In Press, Corrected Proof.

[17] Kocks U.F., Texture and Anisotropy: Preferred Orientations in Polycrystals and their Effect on Materials Properties, Eds. U.F. Kocks, C.N. Tome and H.R. Wenk, Cambridge University Press, 1998, p. 326

[18] Lebensohn, R. A. and C. N. Tomé (1993). "A self-consistent anisotropic approach for the simulation of plastic deformation and texture development of polycrystals: Application to zirconium alloys." Acta Metallurgica et Materialia 41(9): 2611-2624.

[19] Ma, A., F. Roters, et al. (2004). "Numerical study of textures and Lankford values for FCC polycrystals by use of a modified Taylor model." Computational Materials Science 29(3): 353-361.
[20] Wang, H., P. D. Wu, et al. (2010). "A finite strain elastic-viscoplastic self-consistent model for polycrystalline materials." Journal of the Mechanics and Physics of Solids 58(4): 594-612.
[21] Sachs G., Z. Verein. (1928) Deut. Ing., 72 734.
[22] Havner, K. S. (1992). Finite Plastic Deformation of Crystalline Solids, Cambridge University Press.
[23] Kocks U.F., Metall. Trans., 1 (1970) 1121.
[24] Banabic, D., H. J. Bunge, et al. (2000). Formability of Metallic Materials, Springer-Verlag Berlin.
[25] Clausen, B., T. Lorentzen, et al. (1998). "Self-consistent modeling of the plastic deformation of FCC. polycrystals and its implications for diffraction measurements of internal stresses." Acta Materialia 46(9): 3087-3098.
[26] Kröner, E. (1961). "Zur plastischen verformung des vielkristalls." Acta Metallurgica 9(2): 155-161.
[27] Berveiller, M. and A. Zaoui (1979). "An extension of the self-consistent scheme to plastically-flowing polycrystals." Journal of the Mechanics and Physics of Solids 26(5-6): 325-344.
[28] Lebensohn, R. A. and C. N. Tomé (1994). "A self-consistent viscoplastic model: prediction of rolling textures of anisotropic polycrystals." Materials Science and Engineering: A 175(1-2): 71-82.
[29] Lebensohn, R. A. and G. R. Canova (1997). "A self-consistent approach for modelling texture development of two-phase polycrystals: Application to titanium alloys." Acta Materialia 45(9): 3687-3694.
[30] Ahzi, S. and S. M'Guil (2008). "A new intermediate model for polycrystalline viscoplastic deformation and texture evolution." Acta Materialia 56(19): 5359-5369.
[31] e-learning resources for aluminum science and technology (2010), from http://aluminium.matter.org.uk/.
[32] Lopes A. B. (2010) Experimental methods of X-Ray diffraction, lecture notes
[33] Engler, O. and J. Hirsch (2007). "Polycrystal-plasticity simulation of six and eight ears in deep-drawn aluminum cups." Materials Science and Engineering: A 452-453: 640-651.
[34] Choi, S. H., J. C. Brem, et al. (2000). "Macroscopic anisotropy in AA5019A sheets." Acta Materialia 48(8): 1853-1863.
[35] Schmitt, J. H., E. L. Shen, et al. (1994). "A parameter for measuring the magnitude of a change of strain path: Validation and comparison with experiments on low carbon steel." International Journal of Plasticity 10(5): 535-551.
[36] Vieira, M. F. G. (1994). Solicitações Sequenciais em Cobre Policristalino: Comportamento após Pré-deformação. Faculdade de Engenharia. Porto, Universidade do Porto. PhD: 147.
[37] Cao, W. Q., A. Godfrey, et al. (2003). "Annealing behavior of aluminum deformed by equal channel angular pressing." Materials Letters 57(24-25): 3767-3774.
[38] Zhilyaev, A. P. and T. G. Langdon (2008). "Using high-pressure torsion for metal processing: Fundamentals and applications." Progress in Materials Science 53(6): 893-979.

[39] El-Danaf, E. A., M. S. Soliman, et al. (2007). "Enhancement of mechanical properties and grain size refinement of commercial purity aluminum 1050 processed by ECAP." Materials Science and Engineering: A 458(1-2): 226-234.

[40] O'Brien, M. J., H. F. von Bremen, et al. (2007). "A finite element analysis of the superplastic forming of an aluminum alloy processed by ECAP." Materials Science and Engineering: A 456(1-2): 236-242.

[41] Valiev, R. Z. and T. G. Langdon (2006). "Principles of equal-channel angular pressing as a processing tool for grain refinement." Progress in Materials Science 51(7): 881-981.

[42] Ji, Y. H. and J. J. Park (2009). "Development of severe plastic deformation by various asymmetric rolling processes." Materials Science and Engineering: A 499(1-2): 14-17.

[43] Akamatsu, H., T. Fujinami, et al. (2001). "Influence of rolling on the superplastic behavior of an Al-Mg-Sc alloy after ECAP." Scripta Materialia 44(5): 759-764.

[44] Figueiredo, R. B. and T. G. Langdon (2006). "The development of superplastic ductilities and microstructural homogeneity in a magnesium ZK60 alloy processed by ECAP." Materials Science and Engineering: A 430(1-2): 151-156.

[45] Valiev, R. Z. and T. G. Langdon (2006). "Principles of equal-channel angular pressing as a processing tool for grain refinement." Progress in Materials Science 51(7): 881-981.

[46] Segal, V. M. (2004). "Engineering and commercialization of equal channel angular extrusion (ECAE)." Materials Science and Engineering A 386(1-2): 269-276.

[47] Segal, V. M. (2006). "Metal Processing by Severe Plastic Deformation." Russian Metallurgy (Metally) 2006, No. 5, pp. 474–483.

[48] Iwahashi, Y., Z. Horita, et al. (1997). "An investigation of microstructural evolution during equal-channel angular pressing." Acta Materialia 45(11): 4733-4741.

[49] Iwahashi, Y., J. Wang, et al. (1996). "Principle of equal-channel angular pressing for the processing of ultra-fine grained materials." Scripta Materialia 35(2): 143-146.

[50] Jin, H. and D. Lloyd (2004). "The tensile response of a fine-grained AA5754 alloy produced by asymmetric rolling and annealing." Metallurgical and Materials Transactions A 35(3): 997-1006.

[51] Jin, H. and D. J. Lloyd (2005). "The reduction of planar anisotropy by texture modification through asymmetric rolling and annealing in AA5754." Materials Science and Engineering: A 399(1-2): 358-367.

[52] Jin, H. and D. J. Lloyd (2007). "Evolution of texture in AA6111 aluminum alloy after asymmetric rolling with various velocity ratios between top and bottom rolls." Materials Science and Engineering: A 465(1-2): 267-273.

[53] Park, J.-J. and N.-J. Park (2005). "Influence of orthogonal shear on texture and R value in aluminum sheet." Journal of Materials Processing Technology 169(2): 299-307.

[54] Utsunomiya, H., T. Ueno, et al. (2007). "Improvement in the r-value of aluminum sheets by differential-friction rolling." Scripta Materialia 57(12): 1109-1112.

[55] Sidor, J., R. H. Petrov, et al. (2010). "Deformation, recrystallization and plastic anisotropy of asymmetrically rolled aluminum sheets." Materials Science and Engineering: A In Press, Corrected Proof.

[56] Wauthier, A., H. Regle, et al. (2009). "The effects of asymmetrical cold rolling on kinetics, grain size and texture in IF steels." Materials Characterization 60(2): 90-95.

[57] Lee, S. H. and D. N. Lee (2001). "Analysis of deformation textures of asymmetrically rolled steel sheets." International Journal of Mechanical Sciences 43(9): 1997-2015.

[58] Ding, Y., J. Jiang, et al. (2009). "Plastic instability and strain rate sensitivity of ultrafine-grained iron." Journal of Alloys and Compounds 487(1-2): 517-521.

[59] Ding, Y., J. Jiang, et al. (2009). "Microstructures and mechanical properties of commercial purity iron processed by asymmetric rolling." Materials Science and Engineering: A 509(1-2): 76-80.

[60] Lee, K.-M. and H.-C. Lee (2010). "Grain refinement and mechanical properties of asymmetrically rolled low carbon steel." Journal of Materials Processing Technology 210(12): 1574-1579.

[61] Beausir, B., S. Biswas, et al. (2009). "Analysis of microstructure and texture evolution in pure magnesium during symmetric and asymmetric rolling." Acta Materialia 57(17): 5061-5077.

[62] Huang, X., K. Suzuki, et al. (2009). "Microstructural and textural evolution of AZ31 magnesium alloy during differential speed rolling." Journal of Alloys and Compounds 479(1-2): 726-731.

[63] Sidor, J., A. Miroux, et al. (2008). "Microstructural and crystallographic aspects of conventional and asymmetric rolling processes." Acta Materialia 56(11): 2495-2507.

[64] Chang Ha Choi, K. H. K., Dong Nyung Lee (1998). "The Effect of Shear Texture Development on the Formability in Rolled Aluminum Alloys Sheets." Materials Science Forum Texture and Anisotropy of Polycrystals, 273 - 275: 391-396.

[65] Simões, F. J. P., R. J. Alves de Sousa, et al. (2008). "Mechanical behavior of an asymmetrically rolled and annealed 1050-O sheet." International Journal of Mechanical Sciences 50(9): 1372-1380.

[66] Sakai, T., S. Hamada, et al. (2001). "Improvement of the r-value in 5052 aluminum alloy sheets having through-thickness shear texture by 2-pass single-roll drive unidirectional shear rolling." Scripta Materialia 44(11): 2569-2573.

[67] Zuo, F.-q., J.-h. Jiang, et al. (2008). "Shear deformation and grain refinement in pure Al by asymmetric rolling." Transactions of Nonferrous Metals Society of China 18(4): 774-777.

[68] Jiang, J., Y. Ding, et al. (2009). "Mechanical properties and microstructures of ultrafine-grained pure aluminum by asymmetric rolling." Scripta Materialia 60(10): 905-908.

[69] Kim, S.-H., J.-H. Ryu, et al. (2002). "The evolution of shear deformation texture and grain refinement in asymmetric rolling." Materials Science Research International 8: 20-25.

[70] Cui, Q. and K. Ohori (2000). "Grain refinement of high purity aluminium by asymmetric rolling." Materials Science and Technology 16: 1095-1101.

[71] Hielscher, R. and H. Schaeben (2008). "A novel pole figure inversion method: specification of the MTEX algorithm." Journal of Applied Crystallography 41(6): 1024-1037.

Appendix - Calculation of α parameter

In order to calculate α value were used the eq. (2.33):

$$\alpha = \frac{d\varepsilon_p : d\varepsilon_r}{\sqrt{d\varepsilon_p : d\varepsilon_p}\sqrt{d\varepsilon_r : d\varepsilon_r}} \tag{A.1}$$

where ε_p and ε_r being the pre-deformation and reloading strain tensors, respectively. ε_p was determined by the strain matrixes for CR and ASRC below:

$$\varepsilon_{p,CR} = \begin{bmatrix} 1 & 0 & 0 \\ 0 & 0 & 0 \\ 0 & 0 & -1 \end{bmatrix} \tag{A.2}$$

$$\varepsilon_{p,ASRC} = \begin{bmatrix} 1 & 0 & \gamma/2 \\ 0 & 0 & 0 \\ \gamma/2 & 0 & -1 \end{bmatrix} \tag{A.3}$$

where $\gamma = 0.6$, was calculated from macroscopic shear measurements.

ε_r is defined by:

$$\varepsilon_r = \begin{bmatrix} \varepsilon'_{11}\cos^2\theta + \varepsilon'_{22}\sin^2\theta & (\varepsilon'_{22} - \varepsilon'_{11})\cos\theta\sin\theta & \varepsilon'_{13} \\ (\varepsilon'_{22} - \varepsilon'_{11})\cos\theta\sin\theta & \varepsilon'_{11}\cos^2\theta + \varepsilon'_{22}\sin^2\theta & \varepsilon'_{23} \\ \varepsilon'_{31} & \varepsilon'_{32} & \varepsilon'_{33} \end{bmatrix} \tag{A.4}$$

where the θ is the angle between the tensile test direction and rolling direction and ε' depends on the anisotropy coefficient measured for θ:

$$\varepsilon' = \begin{bmatrix} 1 & 0 & 0 \\ 0 & -\dfrac{R_\theta}{1+R_\theta} & 0 \\ 0 & 0 & -\dfrac{1}{1+R_\theta} \end{bmatrix} \tag{0.5}$$

Therefore:

$$\varepsilon_p : \varepsilon = (\varepsilon_{11}\varepsilon'_{11} + \varepsilon_{22}\varepsilon'_{22})\cos^2\theta + (\varepsilon_{11}\varepsilon'_{22} + \varepsilon_{22}\varepsilon'_{11})\sin^2\theta + (\varepsilon_{12} + \varepsilon_{21})(\varepsilon'_{22} - \varepsilon'_{11})\cos\theta\sin\theta + \varepsilon_{13}\varepsilon'_{31} + \varepsilon_{31}\varepsilon'_{13} + \varepsilon_{23}\varepsilon'_{32} + \varepsilon_{32}\varepsilon'_{23} + \varepsilon_{33}\varepsilon'_{33} \quad \text{(A.6)}$$

$$\varepsilon_p : \varepsilon_p = \varepsilon_{11}^2 + \varepsilon_{22}^2 + \varepsilon_{33}^2 + 2(\varepsilon_{12}\varepsilon_{21} + \varepsilon_{13}\varepsilon_{31} + \varepsilon_{23}\varepsilon_{32}) \quad \text{(A.7)}$$

$$\varepsilon : \varepsilon = \varepsilon'^2_{11} + \varepsilon'^2_{22} + \varepsilon'^2_{33} + 2(\varepsilon'_{12}\varepsilon'_{21} + \varepsilon'_{13}\varepsilon'_{31} + \varepsilon'_{23}\varepsilon'_{32}) \quad \text{(A.8)}$$

The α values for the investigated directions are presented in Table 10 and Table 11.

Table 10. Calculated α value of CR samples

θ (°)	R_θ	α
0	0.91	0.88
45	0.7	0.51
90	1.23	-0.06

Table 11. Calculated α value of ASRC samples

θ (°)	R_θ	α
0	1.39	0.78
45	1.24	0.37
90	0.85	0.04